

Babes-Bolyai University
Faculty of Physics

Fabrication and characterization of
FeB NPs for MRI contrast agent
applications

Summary of PhD Thesis

Presented by:

Bogdan Florin Oprea

Scientific Advisor

Prof. Dr. Simion Simon

Cluj-Napoca, October 2013



Universitatea
BABEŞ-BOLYAI



Fabrication and characterization of FeB NPs for MRI contrast agent applications

Summary of PhD Thesis

Cluj-Napoca, October 2013

Table of Contents

I. Objectives and motivation	1
II. Nanoparticles fabrication techniques	3
II.1. Synthesis procedure of FeB NPs	3
II.1.2. Surface functionalization of FeB nanoparticles with polyethylene-glicol	4
II.1.2.1. Directly PEG functionalization on surface NPs deposit	4
II.1.2.2. PEG functionalization of dispersed NPs	4
III. Growth and characterization of FeB nanoparticles	5
III.1. Morphological characterization: AFM	5
III.2. Structural characterization: TEM	6
III.3. Chemical characterization: XPS	7
III.4. Magnetic characterization: SQUID	15
IV. Surface functionalization and characterization of FeB nanoparticles	17
IV.1 FeB NPs surface functionalized directly on the silicon wafer	17
IV.1.1. Chemical characterization: XPS	17
IV.1.1.1. Comparative surface characterization of as deposited/as functionalized FeB NPs.....	17
IV.1.1.2. Depth profile characterization of as functionalized FeB NPs	22
IV.1.2. Structural characterization: Raman	29
IV.2 Dispersed and functionalized FeB NPs for in vitro MRI contrast agent applications	31
IV.2.1. Structural characterization: UV-Vis	31
IV.2.2. Surface charge characterization: Zeta Potential	33
IV.2.3. “ <i>In vitro</i> ” applications: MRI contrast agent	34
IV.2.3.1. Contrast enhancement as a function of NPs concentration	34
IV.2.3.2. Coating influence on contrast enhancement and colloidal stability	36
Conclusions	38
References	

Keywords: FeB, Nanoparticles, Ion Cluster Source, Surface, Depth profile, Superparamagnetism, PEG, Functionalization, MRI contrast agent

I. Objectives and motivation

Metal-borides, such as iron boron particles, present a variety of potential applications like catalysts, magnetic materials, electronic materials etc ¹ thanks to their structural composition and high surface area ^{2,3}. The great advantages of using boron in iron nanoparticles (NPs) have been reported earlier ⁴. In particular, I. Narita et al. showed that the FeB NPs display a higher protection against oxidation and wear and that the insulating character of boron contributes to the reduction of magnetic interaction between NPs.

In the present work the FeB nanoparticles were investigated for their applications as MRI contrast agent. The idea of using NPs based on iron as MRI contrast agent was already discussed ⁵. We first report on the morphological, structural, chemical and magnetic properties of FeB NPs fabricated using an ion cluster source based on the sputtering technique and loaded with a sputtering target with chemical atomic composition Fe₅₀B₅₀. Ion cluster source is a sputtering method for NPs fabrication that has the advantage to be operated under ultra-high vacuum conditions hence allowing high chemical purity. Furthermore the size and flux of NPs are independent of the substrate conditions. The technique allows also the oxidation or nitration of the NPs in a controlled way by tuning the flow of oxygen or nitrogen during or after the deposition process ⁶⁻⁹. Although the reported results in the first part of this study can be regarded as more fundamental than applied, such growth and characterization is necessary for the further use of the NPs in medicine as MRI contrast agent.

In the second step, the NPs surface PEG functionalization process was mandatory in order to avoid the premature clearance from the circulation, caused by the potential lack of biocompatibility or colloidal stability in aqueous solution ^{10,11}. The bounded PEG chains to the NPs surface as well as the changes in chemical and structural were investigated. Two different coating techniques were performed. First, for investigating of the PEG attachment and the changes in structural and chemical properties, the NPs deposit was functionalized directly on SiO_x wafer. In the second step, for investigating the contrast enhancement, the NPs were first separated from the substrate and then coated with polyethylene-glycol.

The in vitro MRI analyses were carried out under an applied magnetic field of 7 T. This fact is important since clinical MRI is evolving also to higher fields for the investigation of nanoparticles as contrast agents ¹². The response of superparamagnetic FeB NPs and PEG FeB NPs as MRI contrast agent is promising for further in vivo study.

The thesis is divided in five chapters, as following:

The first chapter highlights a literature review about the nanoparticles fabrication, superparamagnetic nanoparticles and their applications in biomedical field. In particular, the NPs applications as MRI contrast agent and the factor which influence their efficacy, such as size distribution, biocompatibility, surface modification, were discussed. The existent imaging techniques were also reviewed.

In chapter II present the procedures used for the fabrication (Ion Cluster Source) and coating (functionalization with PEG) of the nanoparticles and some basic principle of the experimental techniques and the equipments used for the analysis of FeB nanoparticles.

Chapter III is focused on the study of the morphological, chemical, structural and magnetic properties of FeB nanoparticles that have been fabricate using an Ion Cluster Source (ICS). A nitrogen flow was used during the deposition process in order to reduce the oxidation level. AFM have been accompanied by transmission electron microscopy (TEM) characterization to investigate the distribution of the obtained nanoparticles in terms of height and diameter respectively. TEM measurements were also used to investigate the crystalline or amorphous nature of the nanoparticles deposit. The elemental composition evolution in depth was characterized by X-ray photoelectron spectroscopy (XPS) measurements, recorded on as deposited sample and after different stages of Ar^+ ions bombardment, until to 490 minutes, corresponding to a depth in range of 0 and 38.5 nm. Superconducting quantum device measurements (SQUID) were involved to investigate the magnetic properties of FeB nanoparticles at room temperature, as well as at low temperature. Two theoretical methods, Langevin fit and Triple fit, were used to determine the superparamagnetic particle size.

In Chapter IV a comparative analysis between uncoated and coated PEG nanoparticles, as well as a depth profile analysis of coated NPs are presented. First, for a better highlighting of PEG attachment and of changes in structural and chemical properties, the NPs deposit, functionalized directly on SiO_x wafer, was investigated. XPS comparative analysis between wide scans and high resolution spectra of uncoated and coated NPs relieves important changes in surface composition and structure. The XPS data were also accompanied by FTIR and Raman structural analyses to confirm the presence of polyethylene (glycol) chains on coated NPs. In depth analysis was used to investigate the structure of coated NPs as well as the thickness of PEG layer bounded to the surface of NPs depozit. The changes which occur in chemical groups, between surface and the interior of functionalized

NPs, were investigated in range of 0 - 19.1 nm distances from surface. In the second step, for investigating the contrast enhancement, we first separate from substrate and then coated the NPs with polyethylene-glycol. The UV-Vis and Zeta Potential measurements on dispersed PEG FeB NPs was involved in order to prove the chemical interactions between the surface of NPs and PEG chains, in good agreement with XPS, Raman and FTIR measurements on functionalized NPs. Three different concentrations of 0.15 mM, 0.30 mM and 0.44 mM were used to investigate the changes in contrast as a function of NPs concentration. For highlighting the effect in terms of contrast after PEG coating, the NPs concentration of 0.30 mM was investigate before and after functionalization. The colloidal stability was also followed as a function of time, after dispersion in the aqueous solution.

Finally, Chapter V highlights the conclusions of this study.

II. Nanoparticles fabrication techniques

II.1. Synthesis procedure of FeB NPs

The samples have been grown at Instituto de Ciencia de Materiales de Madrid, on $10 \times 10 \text{ mm}^2$ silicon wafers and TEM grids using an Ion Cluster Source (ICS) from Oxford Applied Research ⁹ (see figure 1) connected to an ultrahigh vacuum chamber with a base pressure in the low 10^{-9} mbar. The ICS was equipped with a 2 inches magnetron sputtering source loaded with a $\text{Fe}_{50}\text{B}_{50}$ target. The pressure in the aggregation zone and in the UHV system during the deposition process was in the low 10^{-3} mbar and 10^{-5} mbar respectively.

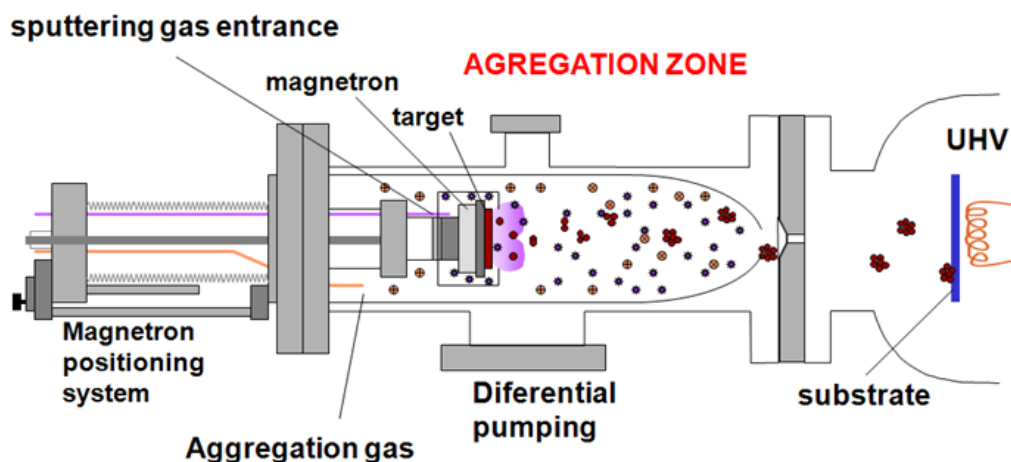


Figure 1: Schematic view of Ion Cluster Source equipment⁷.

II.2. Surface functionalization of FeB nanoparticles with polyethylene-glicol

Taking into account the requirements of the used characterization techniques we performed two different approaches of PEG attachment to FeB NPs.

II.2.1. Directly PEG functionalization on surface NPs deposit

For the characterization of the structural and chemical properties, the nanoparticles were functionalized directly on the SiO_x substrates (see figure 2a). An aqueous solution was prepared by mixing 50 μl of PEG 400 with 5 ml of ultrapure deionized water and, for a better dilution, the mixture was stirred for about 5 minutes. The NPs deposit was suspended in this solution and the interactions between PEG and the top of deposited NPs were allowed to fulfill at room temperature for about 4 h¹³. During this time the mixture was easily stirred. After this process, the deposit was washed for four times in ultrapure deionized water in order to remove the free PEG molecules and dried in the oven (in air) at 37 °C before analysis.

II.2.2. PEG functionalization of dispersed NPs

In case of contrast agent analysis behavior, the NPs deposit was first separated from SiO_x substrate (see figure 2b). The substrate with FeB NPs was introduced in 5 ml ultrapure deionized water and sonicated using a Elma E 60 H Elmasonic ultrasonic bath equipment at room temperature. After the separation from the substrate, the interactions between the NPs were almost negligible and were well dispersed in the aqueous solution. This behavior will be presented in details in Chapter III, where the lack of magnetic interaction will be emphasized.

In order to obtain a relevant comparative image between unbounded FeB NPs and PEG bounded FeB NPs in the same environment, two mixtures were prepared and only one of them was mixed with aqueous PEG solution.

Thus, in the formed ferrofluid 50 μl of PEG 400 were added and the resulted mixture was easily stirred for 4h at room

PEG structure: $\text{H}-(\text{O}-\text{CH}_2-\text{CH}_2)_n-\text{OH}$

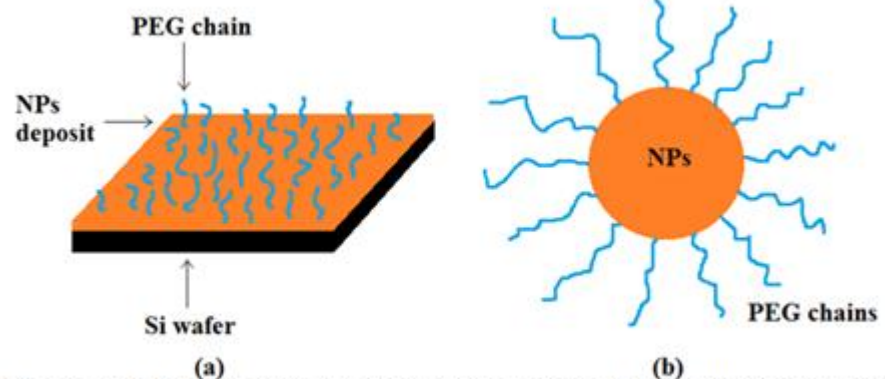


Figure 2: Schematic representation of NPs deposit functionalization (a) and dispersed NPs functionalization (b) processes, with polyethylene-glycol (PEG).

temperature¹³. In order to remove the unbound PEG molecules and to obtain a stable ferrofluid by avoid the eventual aggregation, the solution was then centrifugated using a Micro 22 Hettich equipment, with the speed of 15000 rpm.

III. Growth and characterization of FeB nanoparticles

III.1. Morphological characterization: AFM

AFM was used to characterize the deposits on silicon wafers. The particle height and density were extracted from the AFM images and correlated with the working parameters of the ICS: magnetron power, sputter Ar flow, nitrogen flow and aggregation length, the aperture size being fixed¹⁴. The working parameters were adjusted in order to obtain a high flux of nanoparticles with mean height close to 15 nm. Nanoparticles with such size are likely to present a long enough circulation time in biological media^{15,16} and should display a superparamagnetic behavior like the iron oxide (Fe_3O_4 , Fe_2O_3) nanoparticles with similar size^{15,17}. In Figure 1a we display a representative AFM image that has been recorded on a deposit where the NPs have the size and deposition rate that has been used in the present study. The corresponding working parameters were: 100 mm aggregation length, 100 sccm Ar flow, 0.5 sccm N_2 flow, 43.5 W magnetron power and 30 s deposition time which gave a deposition rate close to $9 \text{ NPs s}^{-1} \cdot \mu\text{m}^2$. The size distribution displayed in Figure 1b has been extracted from several images like the one of Figure 1a. The size distribution of Figure 1b has a total of 767 events distributed in 2 distinct NPs populations and the fit was carried out using lognormal distribution¹⁸. The first population has mean height $h_{\text{mean}} \approx 2.0 \text{ nm}$ and standard deviation $\sigma_h \approx 0.6 \text{ nm}$. This population represents approximately 30% of the total amount of NPs and 0.13% of the total mass. The second population of main interest has a mean height $h_{\text{mean}} = 14.3 \text{ nm}$ and a standard deviation $\sigma_h = 2.6 \text{ nm}$. As deduced from the size distribution, the population of larger nanoparticles is dominant both in number of NPs as well as in mass %. It is expected that in an applied magnetic field, the magnetic signal originated from the smallest nanoparticles will be almost negligible compared to that of larger one.

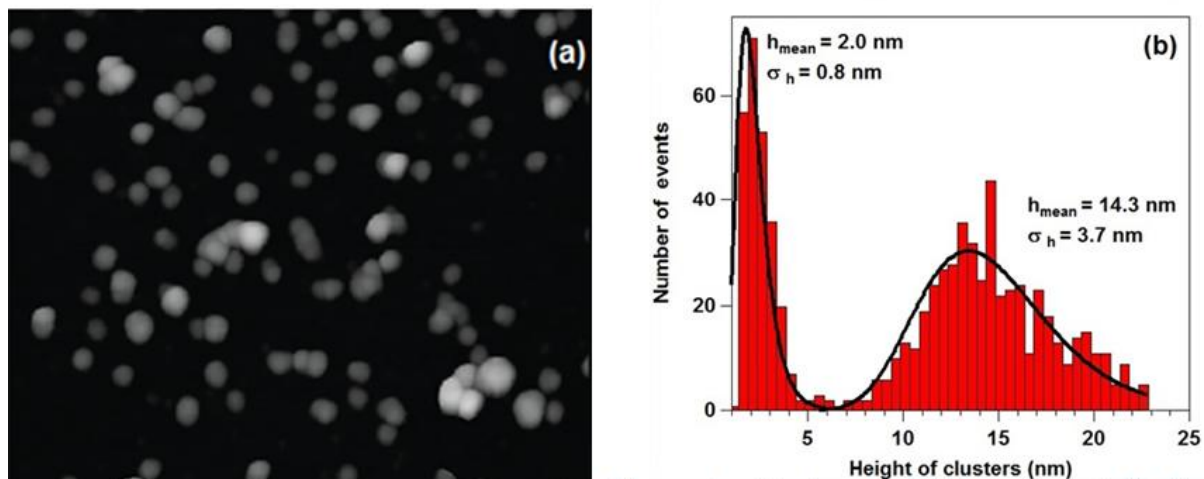


Figure 1: (a) $1 \mu\text{m}^2$ AFM images of $\text{Fe}_{50}\text{B}_{50}$ nanoparticles deposited on silicon wafer substrate; (b) height distribution histogram extracted from three images. The fit of the histogram was carried out assuming a lognormal distribution.

III.2. Structural characterization: TEM

In order to establish the shape of the nanoparticles, TEM measurements have been performed. While AFM is adequate for the measurement of height and density of nanoparticles, it is not reliable for the determination of the diameter due to the inherent convolution between the tip and the nanoparticles¹⁹. Hence, the diameter distribution has been determined using plan-view TEM images such as the one displayed in Figure 2a. TEM images revealed a homogenous diameter distribution and the lack of inter-particles aggregation. The absence of crystalline order was also observed, revealing the amorphous nature of the nanoparticles. Note that such amorphous nature of the $\text{Fe}_{50}\text{B}_{50}$ NPs is comparable to the amorphous nature of iron-boron thin films where the crystalline phase is observable only for iron atomic concentrations above 80%²⁰.

The diameter distribution extracted from the analysis of several TEM images is displayed in Figure 2b. The total number of events used in the size distribution is 315 and, like for the height distribution, a log-normal fit has been applied. The resulting mean diameter and standard deviation are $d_{\text{mean}} = 10.1 \text{ nm}$ and $\sigma_d = 1.8 \text{ nm}$. Taking into account the measured mean height and mean diameter it can be stated, within the measured standard deviations, that the FeB NPs have a spherical shape. The higher deviation between the height and the diameter measured, in comparison to other systems⁷ could arise from the higher hygroscopic character of the FeB NPs that gives slightly higher heights when measured in dynamic mode. This indicates that the nanoparticles are not deformed during the deposition

process, thanks to a “soft landing” as already found in other studies⁷. Due to the low contrast between the graphene coated TEM grids and the FeB nanoparticles, we were unable to observe the population of small nanoparticles.

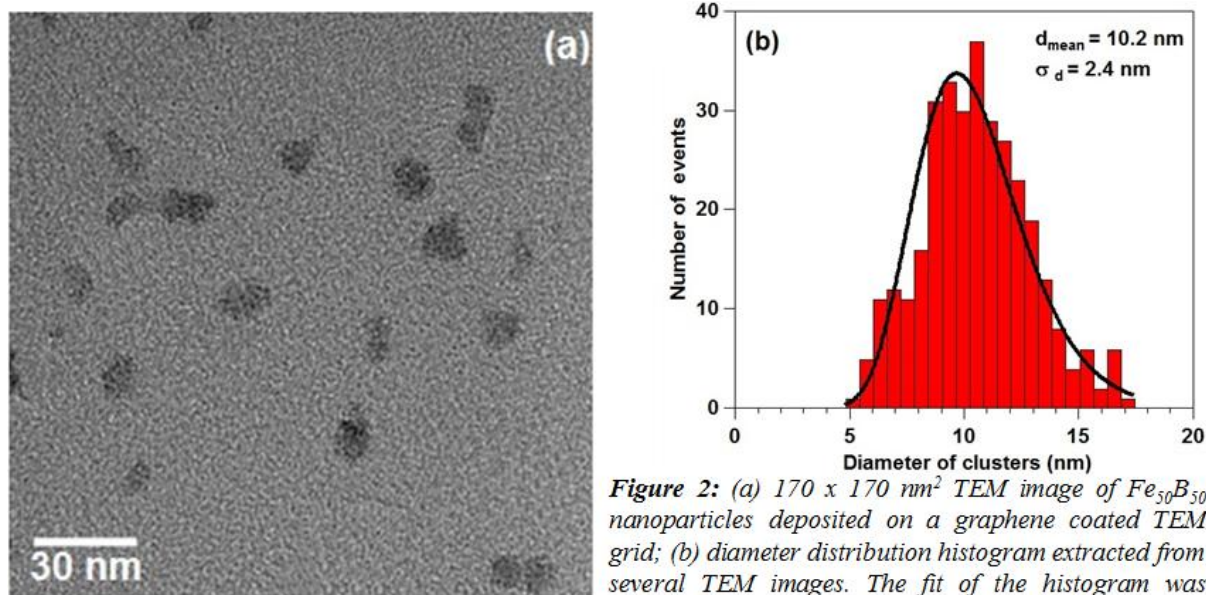


Figure 2: (a) $170 \times 170 \text{ nm}^2$ TEM image of $\text{Fe}_{50}\text{B}_{50}$ nanoparticles deposited on a graphene coated TEM grid; (b) diameter distribution histogram extracted from several TEM images. The fit of the histogram was carried out assuming a lognormal distribution.

III.3. Chemical characterization: XPS

The XPS analysis were performed on a multilayer of FeB NPs in order to minimize the photoemission signal from the silicon wafer. The multilayered nature of the deposit, approximately 350 nm thick, was checked by SEM measurements (see figure 3a). The deposit was transferred from the ICS to the XPS analysis chamber (i.e. exposed to air during the transfer) and measured as grown and after different sputtering times in order to investigate the depth profile chemical composition structure of the NPs. The Ar^+ bombardment or etching was performed up to 490 minutes. The corresponding depth was calculated assuming that the etching rate is similar to the one of FePd compound²¹. Under such assumption, the maximum depth is found to be 38.5 nm. Figure 3b displays the XPS wide-scans for the as deposited sample and at different intermediary depth up to 38.5 nm. The peaks of the elements present in the sample are labeled. As can be observed, the C 1s and O 1s peaks are the most intense ones in the case of as deposited surface (bottom spectrum) as a result of the atmospheric contamination during the sample transfer. Under Ar^+ bombardment, the relative intensities of the XPS peaks corresponding to the other elements increase as a result of the removing of the atmospheric contamination. As can be observed in figure 3, the C 1s peak is till relatively intense even at the maximum distance from the

surface. This is due to the high porosity of the deposit⁸ that allows the deep penetration of the carbon into the multilayer during the sample transfer under atmospheric conditions.

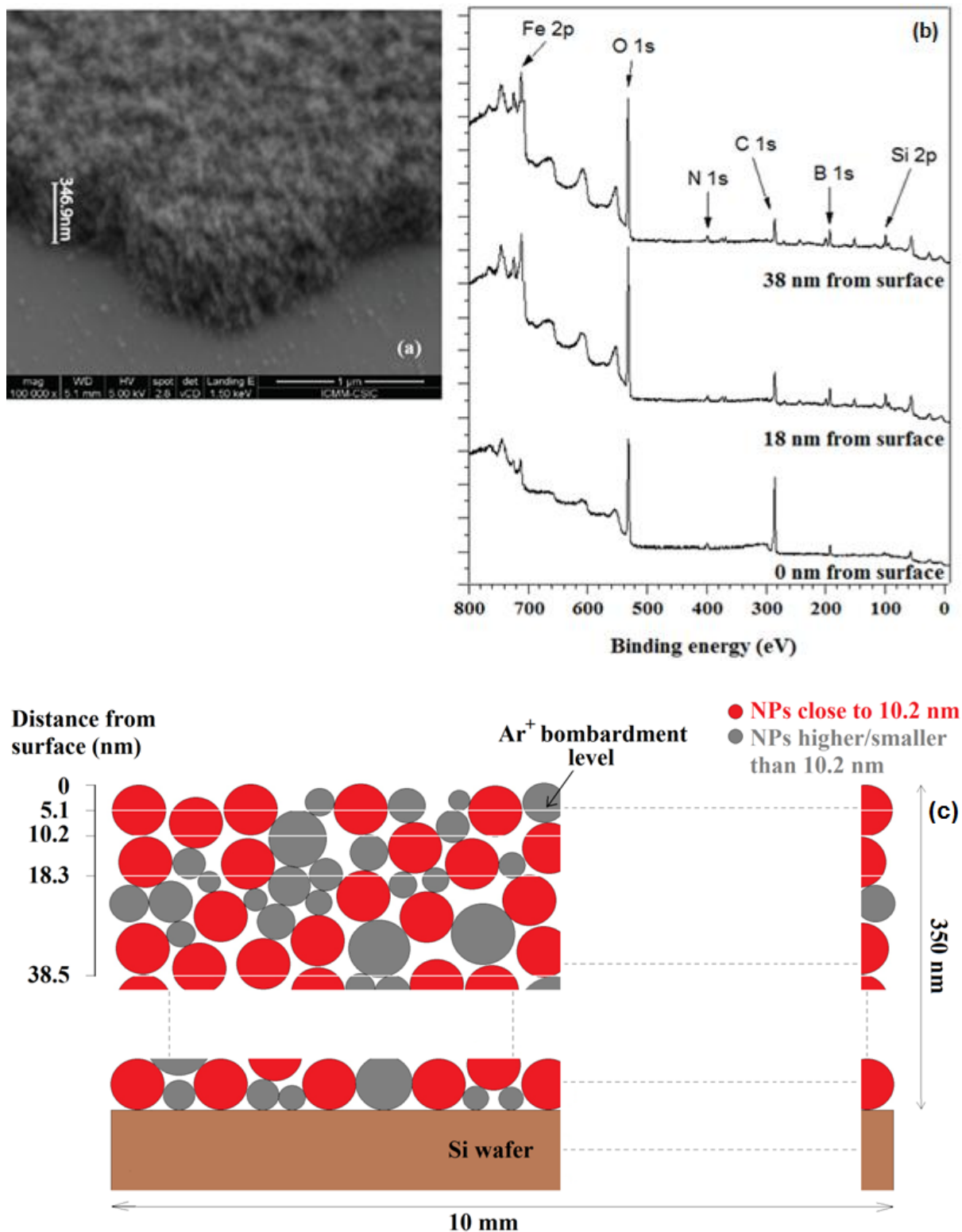


Figure 3: (a) SEM image illustrating the thickness of the $Fe_{50}B_{50}$ nanoparticles deposit on SiO_x substrate; (b) XPS wide scan spectra of FeB NPs deposits as grown and after different sputtering times (c) Schematic view of NPs deposit after different Ar^+ bombardment level.

Before going into the details of the different chemical species present in the sample

as a function of the distance from the surface, we first display in figure 4a the depth profiles of the elements of interest Fe, B, N, O and C (in atomic percentage) extracted from the wide scans like the ones presented in figure 3. In graph of Figure 4a the Si 2p XPS signal was ignored since it does not contain information about the NPs deposit. Although negligible, the O 1s signal contribution from the silicon oxide was also subtracted from the O 1s in the data presented in Figure 4a. This was accomplished thanks to the deconvolution of the O 1s spectra as detailed later. The graph of Figure 4a reveals a very low (close to 3%) and stable content of nitrogen into the multilayer in opposition to the high and strongly decreasing content of carbon as the distance from the surface increases. While the strong decrease of the carbon content can be attributed to the atmosphere contamination²² of the porous multilayer of nanoparticles⁸ the low and stable content of nitrogen is likely to indicate that the small amount of nitrogen is coming from the nanoparticles synthesis. Figure 4a also reveals a similar behavior of the boron, iron and oxygen whose contents slightly increase as a function of distance from the surface and rapidly reach a steady point. Such behavior is consistent with the picture where the oxygen acts as a ligand between iron and boron as previously reported in the literature for the case of Fe₃BO₆ nanorods²³. Also interesting is the dominant concentration of oxygen in all the thickness of the film investigated here except at the outer surface where the carbon contamination is dominant. This clearly reveals that the oxygen has penetrated very efficiently into the nanoparticles multilayer since it is not expected to participate in the fabrication process that is performed under high gas purity. In graph of Figure 4b we have

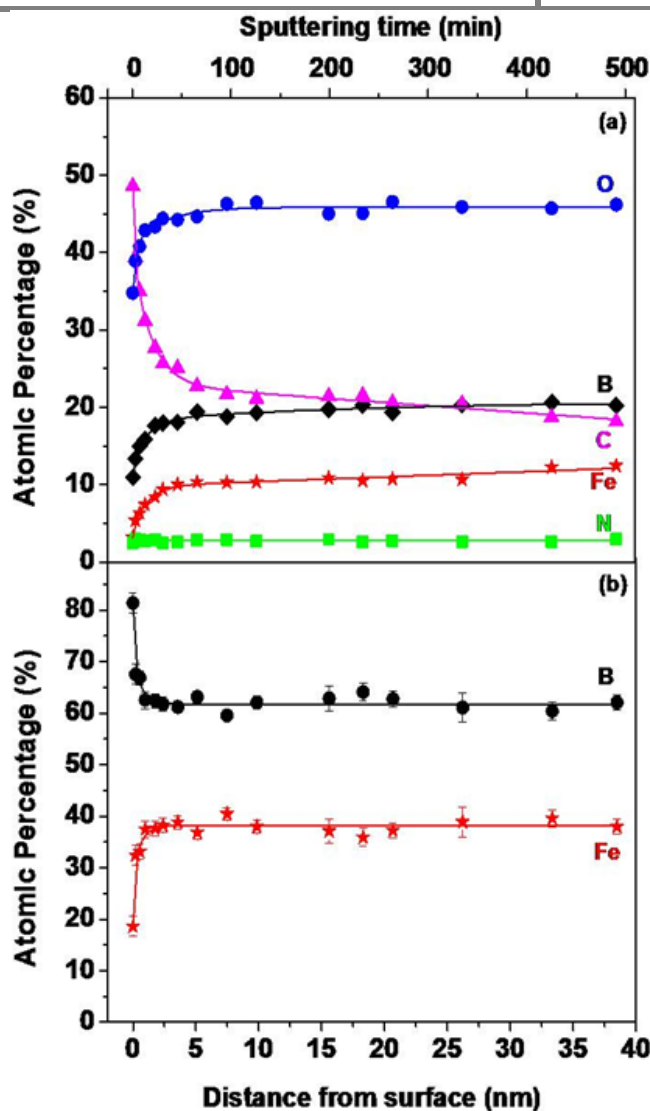


Figure 4: (a) Evolution of the atomic concentration of the most relevant elements as a function of distance from the surface of the multilayer. (b) evolution of the atomic concentration of iron and boron as a function of distance from the surface of the multilayer.

represented the iron and boron atomic concentrations as a function of distance from the surface. In the analysis, the atomic concentrations of the other elements have been ignored. Surprisingly it is observed that the stoichiometric state ($\text{Fe}_{50}\text{B}_{50}$) is never reached, evidencing a boron rich chemical composition that is probably due to the fabrication process and in particular, to a higher sputtering yield for boron than for iron ²⁴.

For a better understanding of the chemical composition of the nanoparticles and its evolution as a function of distance from the surface of the multilayer, we present the detailed analysis of the N 1s, Fe 2p, B 1s and O 1s core levels.

Although small when compared to the other elements (see Figure 4a), it is interesting to investigate the nature of the different components of the N 1s core level peak. As evidenced in Figure 5a, 2 contributions have been identified in the N 1s core level peak spectra measured at the surface of the multilayer, at 18 nm from the surface and at 38 nm from the surface. The most intense contribution that appears at the binding energy of 399.5 - 400 eV can be assigned to the N-O bonds and the less intense component at 398-398.5 eV to the N-B bonds ²⁵. The higher contribution of the N-O bonds is in agreement with the high concentration of oxygen in all the thickness of the film investigated here (see Figure 4a). As it will be shown below, the oxygen bonds with iron and boron are also predominant over other chemical bonds. The profiles of Figure 5b also reveal that the nitrogen is preferentially bonded to oxygen than to boron and that the chemical composition reaches a stable phase at approximately 15 nm from the surface of the multilayer which corresponds roughly to one layer of nanoparticles.

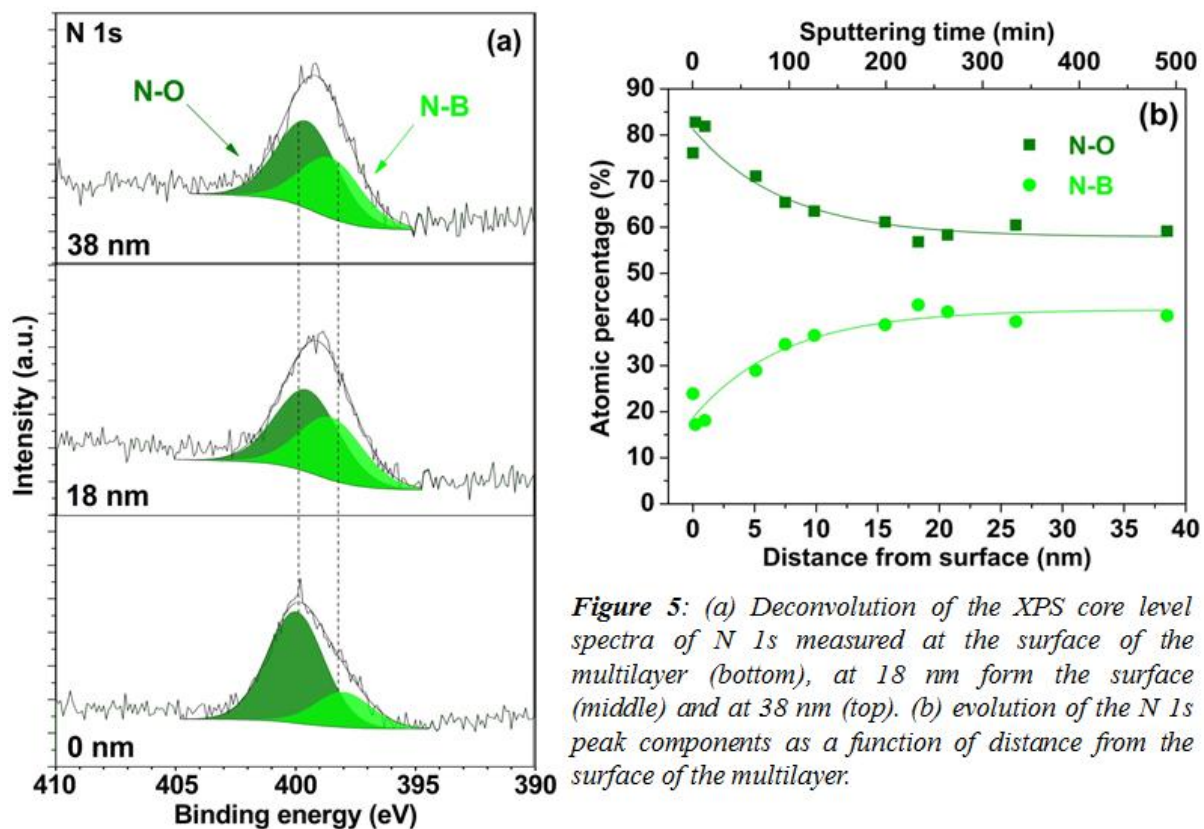


Figure 5: (a) Deconvolution of the XPS core level spectra of N 1s measured at the surface of the multilayer (bottom), at 18 nm from the surface (middle) and at 38 nm (top). (b) evolution of the N 1s peak components as a function of distance from the surface of the multilayer.

We now turn to figure 6 where we display the deconvolution of the Fe 2p core level spectra (Figure 6a) and the resulting evolution of the different species as a function of distance from the surface of the multilayer (Figure 6b). As can be observed in Figure 6a, the shape and binding energy positions of the maxima of the Fe 2p_{1/2} and Fe 2p_{3/2} core levels suffer a strong evolution with the distance from the surface of the multilayer. This clearly indicates the presence of different components in the measured peaks.

Therefore we have fitted the Fe 2p_{1/2} and Fe 2p_{3/2} core levels with different components that in turn have been assigned to Fe⁰, Fe²⁺ and Fe³⁺ species in good agreement with the literature^{23,26-31}. The components labeled a₁ and a₂ correspond to non oxidized iron (Fe⁰ state) while components b₁ and b₂ correspond to Fe²⁺ states. The Fe³⁺ states are represented by c₁ and c₂ components and b₁' and b₂' correspond to satellites structures. As can be observed in Figure 6b, the dominant state is Fe³⁺ along the whole depth profile. At the very first stages of ion sputtering, both Fe²⁺ and Fe³⁺ states suffer important changes in concentration. While Fe³⁺ states concentration stabilizes, the Fe²⁺ states decreases with increasing depth together with an increase in Fe⁰ states that were not present at the surface of the multilayer. As detailed in the discussion, the different iron states suggest that iron atoms do not bond with boron or nitrogen but rather with oxygen in good agreement with the literature³².

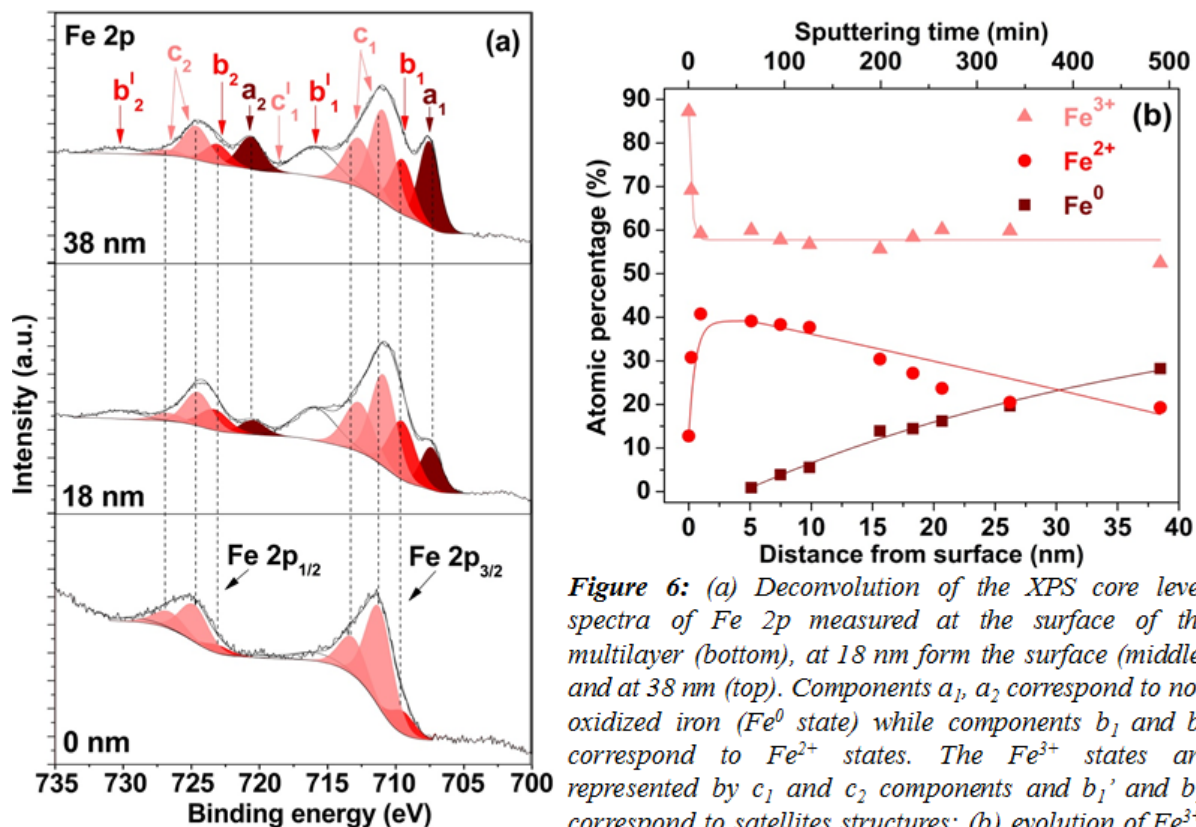


Figure 6: (a) Deconvolution of the XPS core level spectra of Fe 2p measured at the surface of the multilayer (bottom), at 18 nm from the surface (middle) and at 38 nm (top). Components a_1 , a_2 correspond to non oxidized iron (Fe^0 state) while components b_1 and b_2 correspond to Fe^{2+} states. The Fe^{3+} states are represented by c_1 and c_2 components and b_1' and b_2' correspond to satellites structures; (b) evolution of Fe^{3+} , Fe^{2+} and Fe^0 species as a function of distance from surface.

Like for N 1s and Fe 2p core levels, the B 1s core level spectra have been recorded and deconvoluted as can be seen in Figure 7a. Three components have been used in the deconvolution of the B 1s spectra. The component at the lowest binding energy (190.4- 190.6 eV) is attributed to the B-N bonds^{13,33,34} while the component at the highest binding energy (193.4-193.6 eV) is associated to the formation of the stoichiometric B_2O_3 oxide³⁵⁻³⁹. The intermediate component found at 192.2-192.4 eV is associated to the presence of the sub-stoichiometric B_2O_2 oxide^{35,40}. Interestingly, no lower binding energy at around 188 eV associated to B-Fe bonds⁴¹ was observed indicating that boron atoms are preferentially bonded to oxygen and nitrogen atoms rather than to Fe atoms. As can be observed in Figure 7b, the B-N bonds are significantly less abundant than B-O. This fact is not only in agreement with the low concentration of nitrogen in the multilayer but with also previous studies⁴⁰, where this fact was attributed as a result of the thermodynamically less favorable nitriding process of B species than its oxidation. Also remarkable is the constant concentration of B-N bonds along the studied depth. The picture is very different when considering the sub-stoichiometric B_2O_2 and stoichiometric B_2O_3 oxides. While the sub-stoichiometric oxide concentration decreases as a function of distance from the surface, the stoichiometric oxide

concentration suffers the opposite trend revealing a strong variation in oxidation degree of boron as a function of depth into the multilayer.

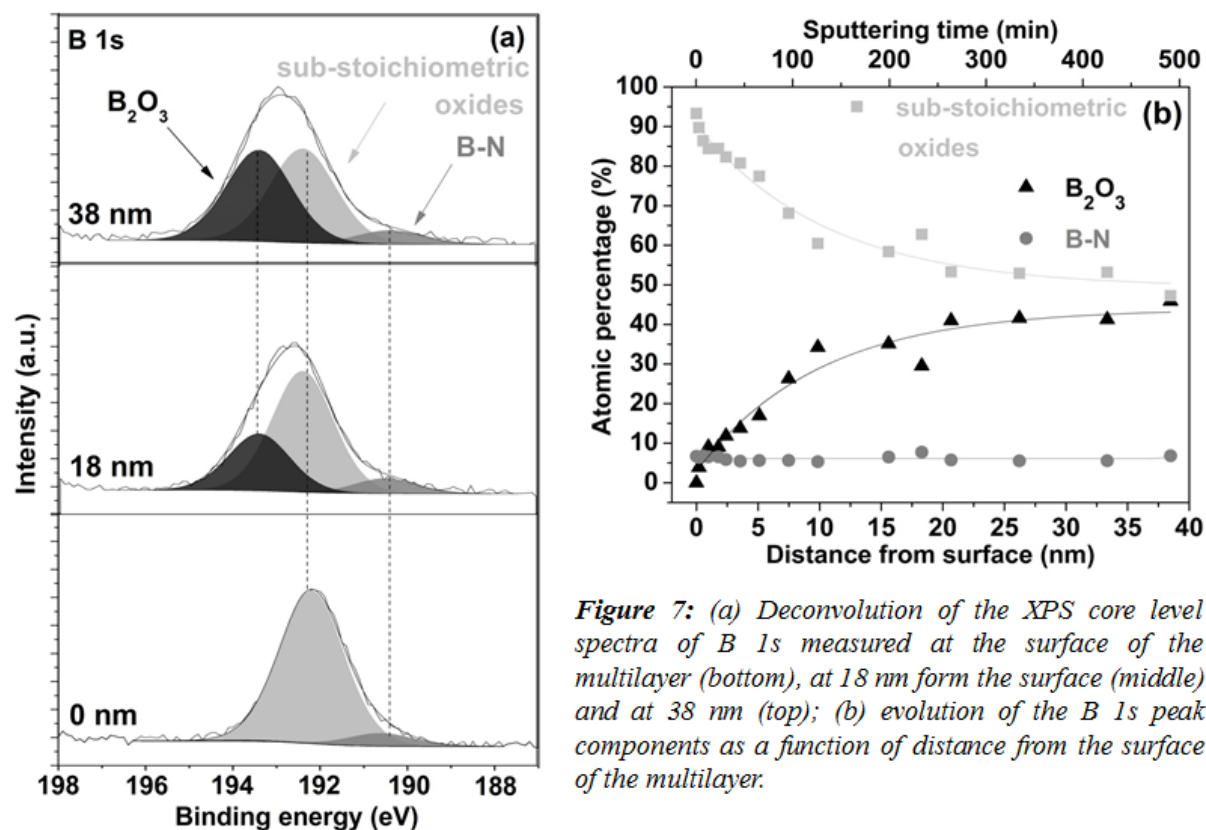


Figure 7: (a) Deconvolution of the XPS core level spectra of B 1s measured at the surface of the multilayer (bottom), at 18 nm from the surface (middle) and at 38 nm (top); (b) evolution of the B 1s peak components as a function of distance from the surface of the multilayer.

We finally go through the O 1s core level spectra and their deconvolution displayed in Figure 8a. Reasonable fits of the O 1s core level could be obtained using 4 components. The component with lowest binding energy (530.4 ± 0.1 eV) was found only close to the surface of the multilayer and was assigned to stoichiometric metal oxides (in our case O-Fe bonds)³¹. The component located at a binding energy of 531.5 ± 0.2 eV was found at all thicknesses and was attributed to the presence hydroxyl OH^- groups⁴² although it could also account for the presence of defects⁴³⁻⁴⁶. Also, a component compatible with the presence of boron oxides^{35,47,48} was found at a binding energy of approximately 532.5 eV. Finally a fourth component with highest binding energy of 533.7 ± 0.1 eV was necessary for the fitting of the O 1s core level spectra. This last component is compatible with the presence of O-N bonds⁴⁹. As can be seen in Figure 8b, the intensity of component O-Fe decreases rapidly as a function of distance from the surface of the multilayer and become negligible. Also the component related to the O-N bonds is relatively small as expected from the low concentration of nitrogen in our system (cf. Figure 4). On the other hand, it appears that the OH^- , B-O oxides components are dominant in the multilayer with rather constant intensities except at the surface of the multilayer where their intensities increase rapidly.

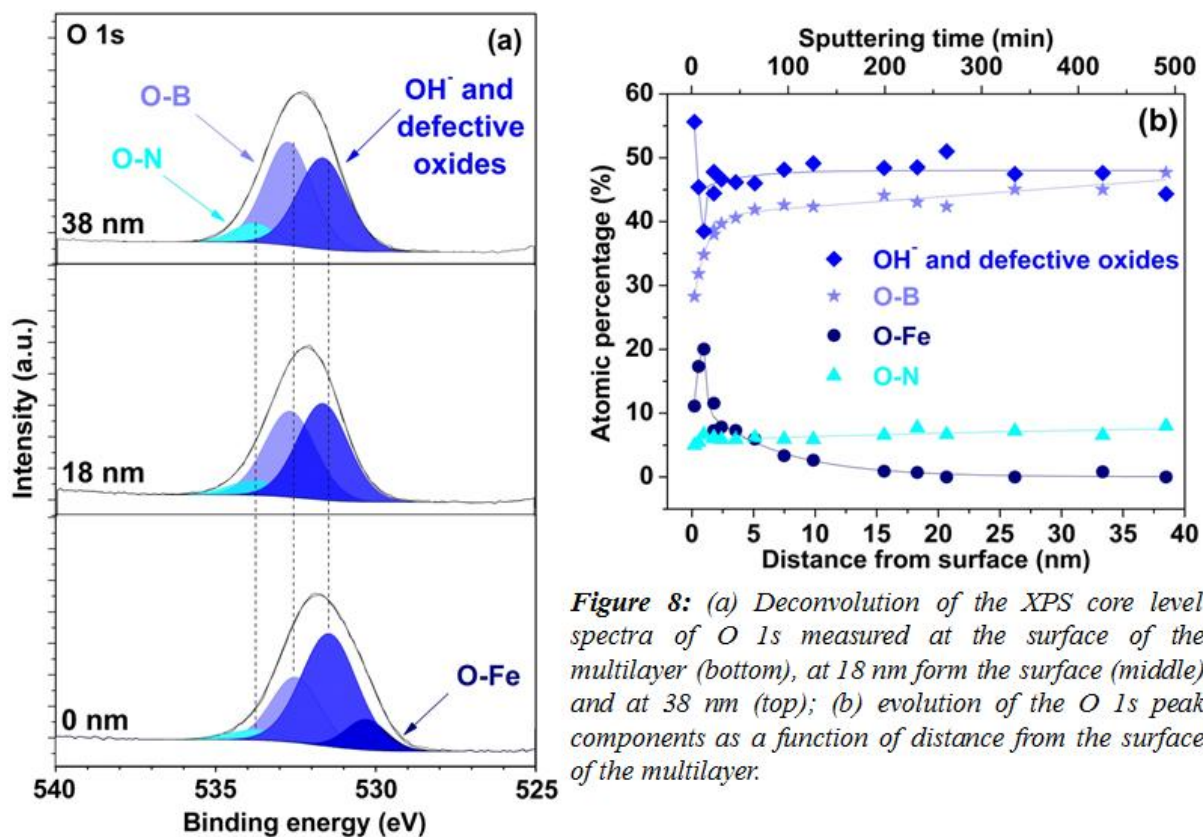


Figure 8: (a) Deconvolution of the XPS core level spectra of O 1s measured at the surface of the multilayer (bottom), at 18 nm from the surface (middle) and at 38 nm (top); (b) evolution of the O 1s peak components as a function of distance from the surface of the multilayer.

In summary, from the XPS analysis we observed that this is a rather complex system mainly formed by boron and iron oxides. No Fe-B bonds were found so it seems that these elements are not forming the same compound. Previous studies reported the possibility of oxygen acting as ligand between Fe and B (forming Fe_3BO_6)²³. However, we were not able to unequivocally confirm the presence of such compound in our system. In addition, nitrogen was found to be bonded only to O and B. According to Xie et al.⁴⁰, we can consider the formation of a $\text{B}_2\text{O}_{3-x}\text{N}_x$ compound. If we assume that all N of the system is forming this boron oxynitride (as no evidences of Fe-N bonds were found) and all sub-stoichiometric boron oxide (fig. 7) is forming this compound, it is possible to extract the x value after each XPS measurement. The x value obtained was 0.4 ± 0.1 throughout the sputtering, leading to a boron oxynitride with an stoichiometry $\text{B}_2\text{O}_{2.6}\text{N}_{0.4}$.

Therefore, from the XPS analysis we observed that, even though most of the Fe and B are bonded to oxygen, the proportion of oxygen in from of iron oxides is rather small and cannot fully explain the amount of Fe^{2+} and Fe^{3+} . As an attempt to clarify whether the component at 531.5 eV in the O 1s core level peak is mainly due to OH⁻ species or due to the presence of oxygen vacancies in the oxide, in a first approximation we calculated the O/(Fe+B) ratio considering the at% of O, Fe and B extracted from the wide scan (Figure 4). The results are plotted in figure 9a. If all oxygen exists in form of O^{2-} , this ratio should be 1.5

for their higher oxidation states (Fe_2O_3 and B_2O_3 , respectively). However, supposing that these elements were in the hydroxide form ($\text{Fe}(\text{OH})_2$ and $\text{B}(\text{OH})_3$) and considering that the amount of B doubled the Fe one, the minimum O/(Fe+B) ratio should be around 2.7. In our system, this ratio varies between 2.5 on the top surface and 1.4 at 38.5 nm from the surface.

A ratio of 2.5 represents around the 80% of the oxygen in hydroxide form. With the sputtering process, the O/(Fe+B) ratio rapidly decreased and at 2.4 nm from the surface, the hydroxide content is below 10% (1.6 ratio). At deeper analysis the ratio reached values lower than 1.5, suggesting that no contribution arises from hydroxides. If we compare these calculations with the assignation of the components on the analysis of the O 1s core level peak (Figure 8), it is evident that the component at 531.5 eV cannot be attributed exclusively to the presence of hydroxides, especially on deeper analysis where the apparent contribution of the OH^- in the O/(Fe+B) is null while the component at 531.5 eV of the O 1s is predominant. In fact, in the spectrum displayed in figure 8a for the analysis at 18 nm, the component due to O-Fe bonds have already disappear and from the O/(Fe+B) ratio calculated we observed that no hydroxide contribution is found at this depth. Therefore, we can conclude that hydroxides are present just on the first 15 nm (approximately the first NPs layer). After that, the whole contribution of the component at 531.5 eV has its origin in defective oxides and in particular Fe oxides.

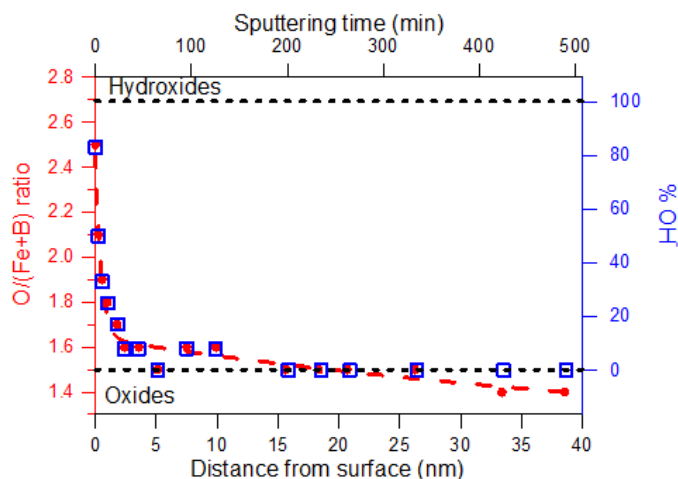


Figure 9: Evolution of the O/(Fe+B) ratio and equivalent proportion of hydroxide in the system as a function of distance from the surface of the multilayer.

III.4. Magnetic characterization: SQUID

SQUID measurements were performed on a sample with high density deposit in order to investigate the magnetic properties of the assembly of NPs¹⁹.

Figure 10 displays the hysteresis loops measured at room temperature and 10 K after zero field cooling (ZFC). As can be observed, the NPs show a superparamagnetic behavior at room temperature and a weak ferromagnetism at 10 K.

The evolution of the magnetization as a function of temperature in ZFC and FC conditions was also investigated as can be seen in Figure 11.

From the curves of Figure 11, a well-defined blocking temperature (temperature limit above which superparamagnetic behavior appears and where the magnetization of the NPs is free to align with the applied field⁵⁰) of approximately 17.5 K is found. These results clearly show that the NPs can be used in medical applications where the superparamagnetic behavior is a key requirement.

For a better understanding of the interparticles interaction, the determination of superparamagnetic particle size is vital for later applications. Two theoretical methods were chosen to calculate this. A good way to perform that is to represent the experimental normalized magnetization measured at room temperature and the Langevin fit. Taking into account the maximum magnetization saturation, the Langevin function fit was carried out using the procedure described in literature⁵¹. The second method used is the Triple Fit and was performed likewise, using the procedure described in literature in which simultaneous triple adjustment is applied to the experimental magnetization curve⁵². From both techniques, it was found that the superparamagnetic nanoparticles size is ≈ 2.9 nm,

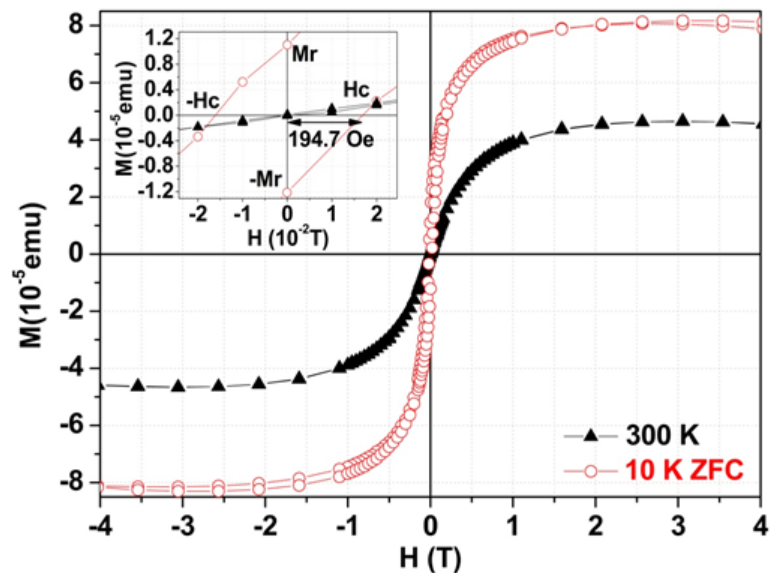


Figure 10: Magnetization as a function of applied magnetic field (B - H hysteresis loop) at room temperature in a applied magnetic field of 50 kOe versus ZFC magnetic field-dependent magnetization curves for FeB samples measured at low temperature (10K) in an applied field of 50 kOe. In the inset is presented a zoom displayed a small coercive field with a small remanent magnetization at room temperature versus magnetization remanence and coercive field at ZFC.

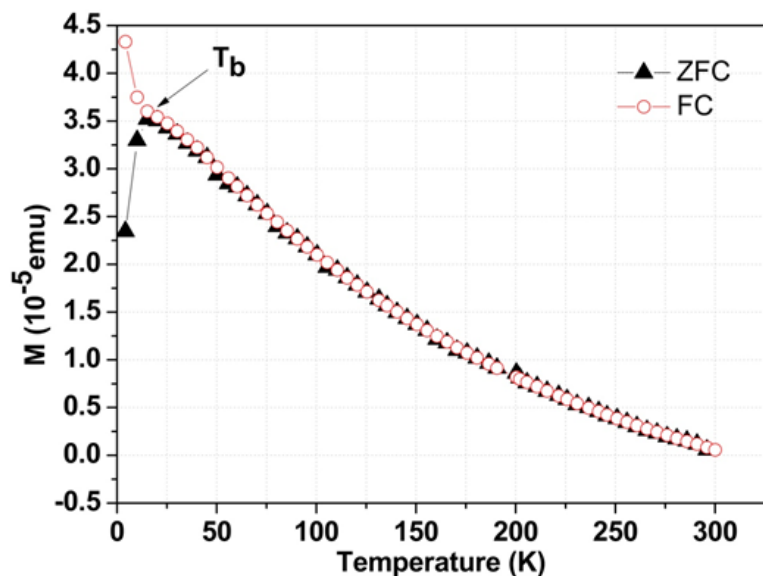


Figure 11: Temperature dependence of magnetization for FeB nanoparticle under ZFC (black line) and FC (red line) conditions, at applied magnetic field of 1.5 kOe.

which means that it is smaller than 9 nm, the superparamagnetic iron limit reported in the literature⁵³. These results confirm that at room temperature the majority of the nanoparticles do not interact with each other, as can be shown in figure 10.

The interactions or non-interactions between FeB nanoparticles were well proved also by the values of magnetic remanence at low temperature, after the applied magnetic field is decreased. The Stoner-Wohlfarth model reveals that the nanoparticles which are close to each other, are exchange coupled, and the nanoparticles at large distance are magnetostatically coupled. The difference between these two situations can be highlighted by the value of magnetization remanence. If the ratio between the magnetization remanence and magnetization saturation is higher than 0.5, this is a proof of the exchange coupling existence and if the ratio is smaller than 0.5, the nanoparticles are magnetostatic coupled. In our case such ratio is much smaller than 0.5, as a consequence of a very low magnetic interactions between FeB nanoparticles. These results are in good agreement with XPS analysis for as deposited sample where it has been shown that, on the NPs surface the quantity in atomic percentage of iron is around 18.6% while boron is around 81.4%. As a consequence the nanoparticles are randomly oriented with uniaxial anisotropy before or after applying a magnetic field.

IV. Surface functionalization and characterization of FeB nanoparticles

IV.1 FeB NPs surface functionalized directly on the silicon wafer

IV.1.1. Chemical characterization: XPS

IV.1.1.1. Comparative surface characterization of as deposited/as functionalized FeB NPs

Using the same procedure like in case of as deposited FeB NPs (see section III.3, Chapter III), elemental surface and in depth composition were determined by XPS analysis. Due to the use of silicon wafers as substrate for depositing of NPs, the surface analysis were performed on PEG coated FeB multilayers NPs, in order to minimize the photoemission signal of Si. The deposit was measured after functionalization²² and proofs of PEG attachment to the surface of FeB NPs were further discussed. Analysis at different distances from surface were also performed in order to confirm the changes in chemical composition of functionalized NPs with depth and to try to determine the thickness of bounded PEG layer

from the top of NPs. The Ar^+ bombardment or etching was performed up to 235 minutes. Assuming the same etching rate as for FePd compound⁵⁴ we found the individual depth for each sputtering time and the total depth was calculated to be 19.1 nm.

Figure 1a shows the wide scans of as deposited sample before and after surface functionalization with PEG. The most dominant contributions in both overlapped wide scans are the O 1s and C 1s peaks. This is an evidence about the level of contamination at the surface of deposit²², which remain still high after the functionalization process. That behavior can be related with air exposure before the analysis, in both cases. The atomic percentages analysis reveals important changes in terms of structure during the functionalization process. We can observe a clear decrease of surface boron amount after functionalization, to 2.0%, comparing with the corresponding amount from as deposited sample of 13.1%. From UV-Vis analysis (see figure 1b) made on the solvent in which NPs were functionalized, we found a consistent presence of boron⁵⁵, which is an evidence of the dissolution of a boron quantity from the surface of NPs during functionalization and explains the decrease of boron concentration from NPs deposit after this process. As a consequence of boron dislocation, the iron amount increases on the NPs surface from 3.0% to 6.0%. If the concentration of nitrogen doesn't change too much and slightly decreases from 2.6 % to 1.9 % after PEG attachment, the atomic concentrations of oxygen and carbon increase after functionalization from 33.6 % and 47.6% to 37.0% and 53.1% respectively. Since the structure of PEG chains contains bonds based on oxygen and carbon, the increase of the concentration of these elements could be related with the attachment of PEG on the NPs, as we will discuss in the following.

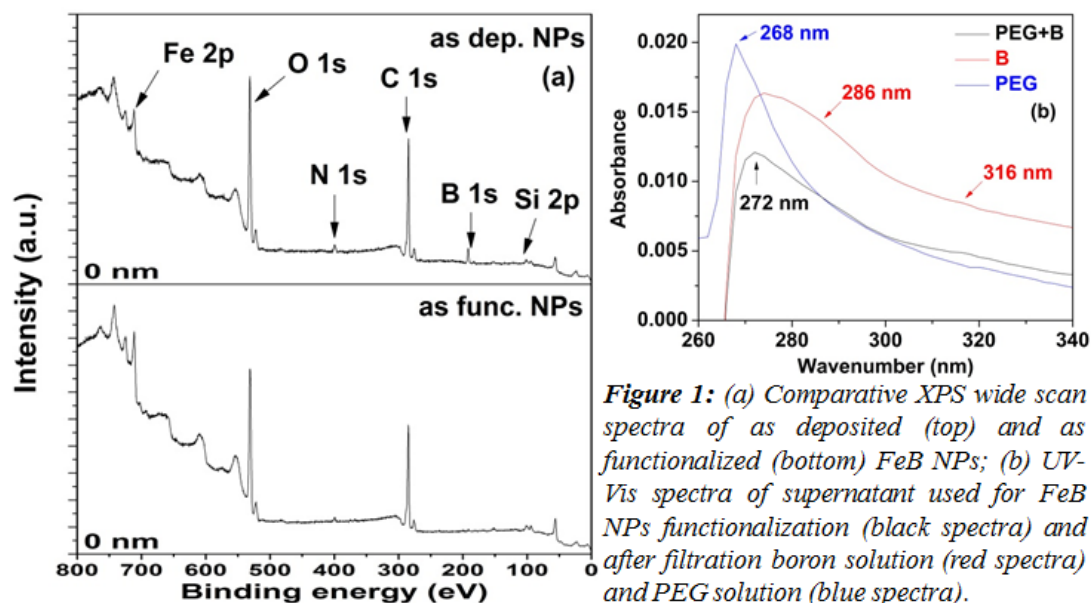


Figure 1: (a) Comparative XPS wide scan spectra of as deposited (top) and as functionalized (bottom) FeB NPs; (b) UV-Vis spectra of supernatant used for FeB NPs functionalization (black spectra) and after filtration boron solution (red spectra) and PEG solution (blue spectra).

For a better understanding of the surface changes in terms of structure during the functionalization, high resolution spectra of all the elements of interest were recorded and Lorentzian-Gaussian deconvolution for each of them were performed.

In figures 2a, b and c we present the deconvolutions of high resolution spectra of Fe 2p, B 1s and N 1s. Although in this peaks there is no any important proof about the attachment of PEG during the functionalization process, important changes at the Fe and B core levels are observed. The spin-orbit distance between Fe 2p_{3/2} and Fe 2p_{1/2} was found to be 13.6 eV⁵⁶ for both spectra (figure 2a). As already done for as deposited sample (see section III.3, Chapter III), the Fe 2p_{1/2} and Fe 2p_{3/2} core levels for as functionalized sample were deconvoluted taking into account the existence of three different species of iron, Fe⁰, Fe²⁺ and Fe³⁺^{23,27-31}, which emphasize different levels of iron oxidation (see figure 2a). All these iron species were well fitted considering the separation in binding energy between Fe⁰, Fe²⁺ and Fe³⁺ and the position in XPS spectra. At the Fe 2p_{3/2} core level it has been found that the contribution from 707.5 eV corresponds to non-oxidized iron Fe⁰, Fe²⁺ oxidized iron where represented by the peak from 709.5 eV and Fe³⁺ oxidized state were composed by two peaks at 711.2 eV and 713.2 eV. In as functionalized sample a dominant contribution of Fe³⁺ and a low concentration of Fe²⁺ were found. However a decrease in the oxidation level as compared with the as deposited NPs (where no evidence of this contribution was observed), is evidenced by the presence of a small amount of non-oxidized Fe⁰.

One of the most important change observed in as functionalized NPs structure is related with the evolution of the boron concentration, which influence also the evolution of

the iron content in the NPs structure. In figure 2b we display the deconvolution of high resolution spectra of B 1s before and after functionalization. In good correlation with the as deposited high resolution spectra, we considered the possible existence of two different boron species in as functionalized sample spectrum, sub-stoichiometric B-O and B-N groups, with their corresponding binding energies positions. The small peak which appear at lowest binding energy, at 190.6 eV was assigned to B-N bonds^{25,33,34} in agreement with the low concentration of nitrogen. As observed in the wide scans of figure 1, the boron concentration decreases dramatically after the functionalization process. The amount of sub-stoichiometric oxides from as functionalized sample, which occurs at 192.2 eV^{35,37,40}, confirms and clarifies this behavior. As can be observed in figure 2b, comparing with the as deposited sample, it is obvious that B-O sub-stoichiometric oxide contribution decreases dramatically while B-N content slightly decreases and do not display significant changes after PEG attachment.

Figure 2c presents the changes related with the structure of nitrogen after functionalization. Deconvoluted high resolution spectra of N 1s for as deposited and as functionalized samples are compared. Although the nitrogen contribution at the surface of NPs was very low in as deposited sample (< 3%), its contribution is very important for further applications taking into account that changes in its concentration or structure influence the oxidation level of the deposit. With a slightly symmetric decrease caused by the functionalization process, the chemical structures of nitrogen display the same structural groups. The most intense contribution represented by N-O bonds appears at 400 eV and the less intense component corresponding to N-B bonds appears at 398 eV²⁵. No significant change observed after PEG attachment.

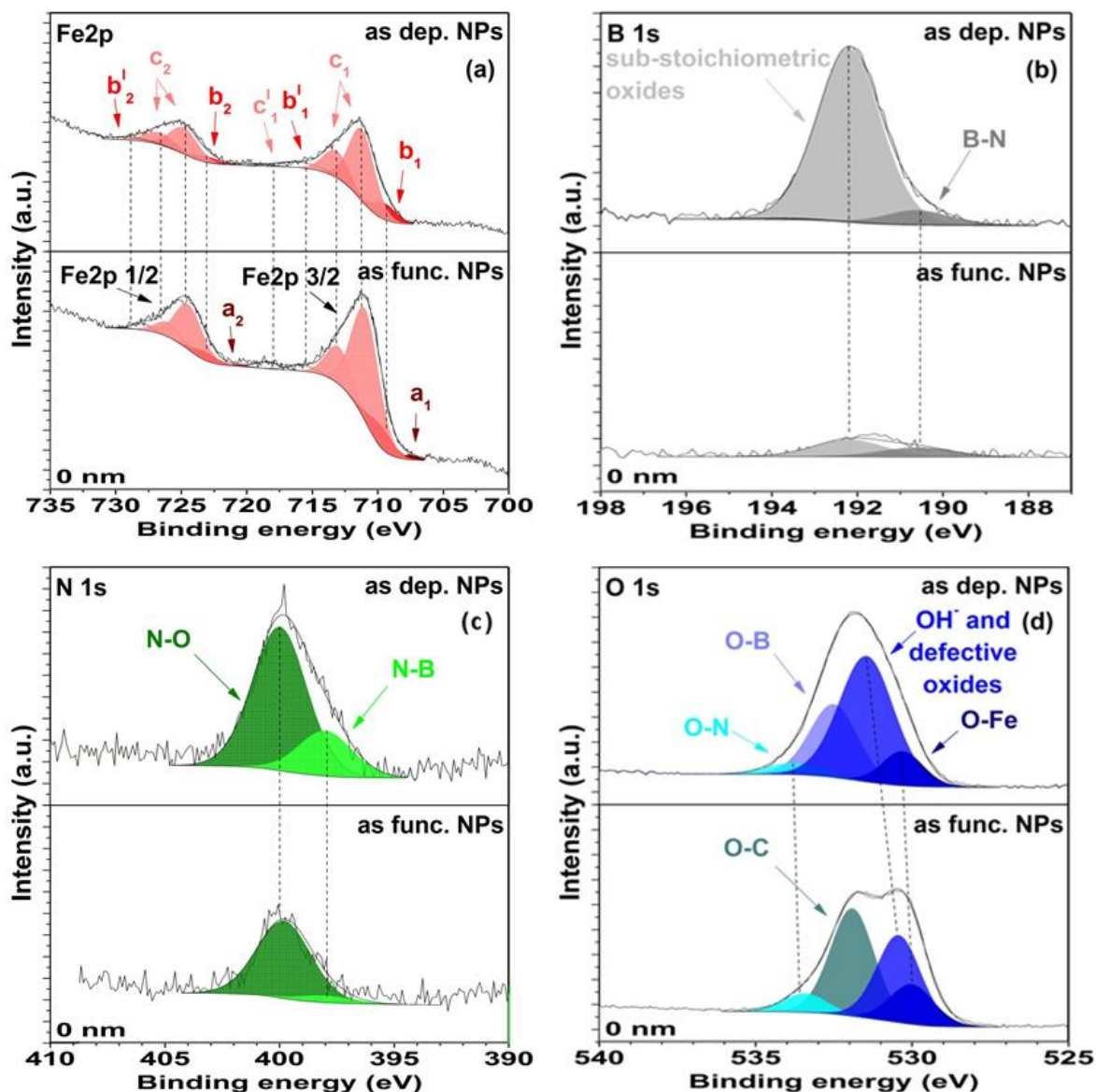


Figure 2: (a) Comparative deconvolutions of the XPS core level spectra of Fe 2p measured on as deposited (top) and as functionalized (bottom) FeB NPs. Components a_1 , a_2 correspond to non oxidized iron (Fe^0 state) while components b_1 and b_2 correspond to Fe^{2+} states. The Fe^{3+} states are represented by c_1 and c_2 components and b_1' and b_2' correspond to satellites structures; (b) Comparative deconvolutions of the XPS core level spectra of B 1s measured on as deposited (top) and as functionalized (bottom) FeB NPs; (c) Comparative deconvolutions of the XPS core level spectra of N 1s measured on as deposited (top) and as functionalized (bottom) FeB NPs; (d) Comparative deconvolutions of the XPS core level spectra of O 1s measured on as deposited (top) and as functionalized (bottom) FeB NPs;

The deconvolutions of Fe 2p, B 1s and N 1s high resolution spectra have shown that the functionalization does not change the chemical bonds in the NPs, i.e. iron atoms are bonded to oxygen, boron atoms form bonds with oxygen and nitrogen rather than with iron atoms, and nitrogen atoms are bonded to oxygen and boron³².

The most important changes which confirm the PEG chain attachment to the NPs deposit are evidenced through the deconvolution of O 1s high resolution spectra. By

comparing the deconvoluted oxygen structures, we could distinguish different species inside the O 1s envelope (see figure 2d). As we already discussed in section III.3 of Chapter III, the O 1s peak of as deposited sample was deconvoluted with four peaks, taking into account the possible bounds which can form the NPs structure. The dominant contribution was assigned to OH⁻ bonds, which appear at 531.45 eV⁴². Another important concentration at 532.50 eV was assigned to O-B bonds like in other works^{35,47,48}, and in good correlation with the expected amount from survey scans. The peak located at lower binding energy value, close to 530.30 eV, is attributed to the stoichiometric metal oxides O²⁻ contribution (O-Fe bonds)^{13,23,31}. At higher binding energy values, around 533.75 eV, a low intensity band complete the deconvolution⁴⁹ and was assigned to O-N bonds. By comparing the O 1s high resolution spectra, before and after functionalization, we observe an important change on the O-B group, that is too low and too close to O-N and O-C contributions to be identified after PEG attachment. This is a consequence of boron dissolution and increase of a new band at 531.90 eV, close to the one of O-B bonds, attributed to O-C oxygens⁵⁷ from PEG chain. There are also significant changes which occur at the O 1s core levels after functionalization. The O²⁻ oxygens contribution is shifted 0.3 eV to 530.00 eV, close to the value of stoichiometric O²⁻^{13,23,31}, and OH⁻ oxygen contribution is shifted 1.05 eV to 530.40 eV. These last binding energy shifts are related with the carbonates formation caused by the chemical interaction with PEG chains⁵⁸. The O-N band appears after PEG attachment at 533.40⁴⁹, shifted with 0.35 eV as compared with as deposited sample. That last shift could attributed to defective oxides, PEG chains interaction or to a small boron oxide contribution inside this envelope. After PEG attachment the O-N component appears slightly increased in O 1s deconvoluted peak. This is unusual taking into account the lower concentration of nitrogen after functionalization. Therefore, the shift to lower binding energy is more likely to be caused by a small boron oxide contribution.

IV.1.1.2. Depth profile characterization of as functionalized FeB NPs

For a better understanding of the chemical changes as a consequence of the functionalization of the NPs and also for a better estimation of the thickness of PEG layer bounded to the surface of the deposit, XPS depth profile were performed.

XPS wide-scans of NPs functionalized directly on the substrate with PEG, recorded on the surface and after different distance from surface, are presented in figure 3. The

concentrations of C 1s and O 1s on the surface are the most visible in part as a consequence of air exposure after deposition and functionalization processes.

Figure 4a emphasizes the elemental evolution with depth. The high and constant O 1s concentration is the consequence of the presence of different species of oxygen on the surface and inside of the NPs, as we will see later. The concentration of C 1s decreases with depth due to the progressive removal of contamination and PEG layer. Even in that situation, inside of the deposit we still have a high concentration of carbon⁸ which proves the porosity of the deposit. There is no important evolution of the nitrogen content during the functionalization process.

The evolution of Fe and B concentrations excluding the other elements and as a function of distance from surface is given in figure 4b. Despite the decrease of boron concentration to 25.3% after PEG attachment (in as deposited sample it was 81.4%), the trend as a function of distance from surface is the same as in case of as deposited samples, i.e. an increase of the iron amount together with a decrease of the boron content.

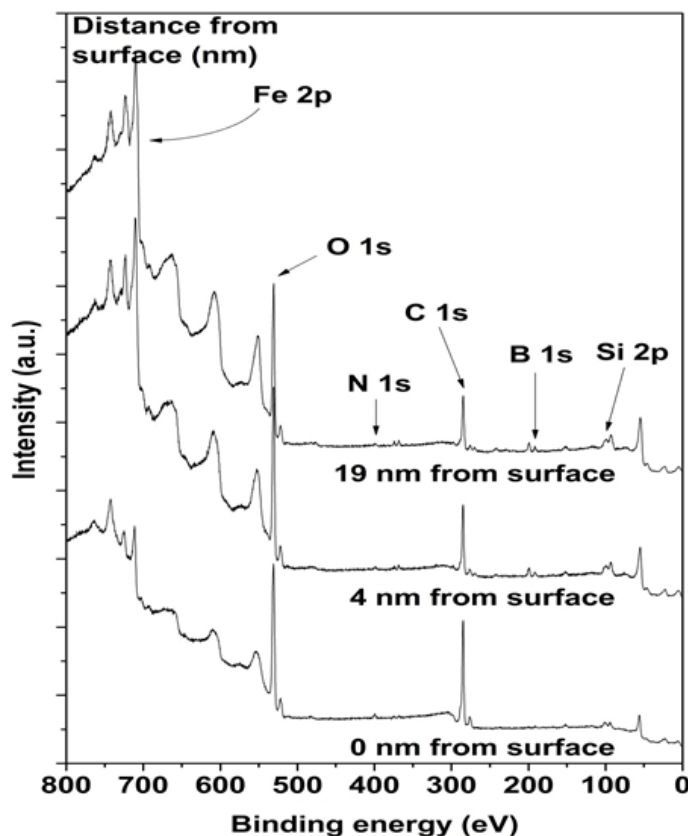


Figure 3: XPS wide scan spectra of as functionalized FeB NPs deposits as grown and after different sputtering times.

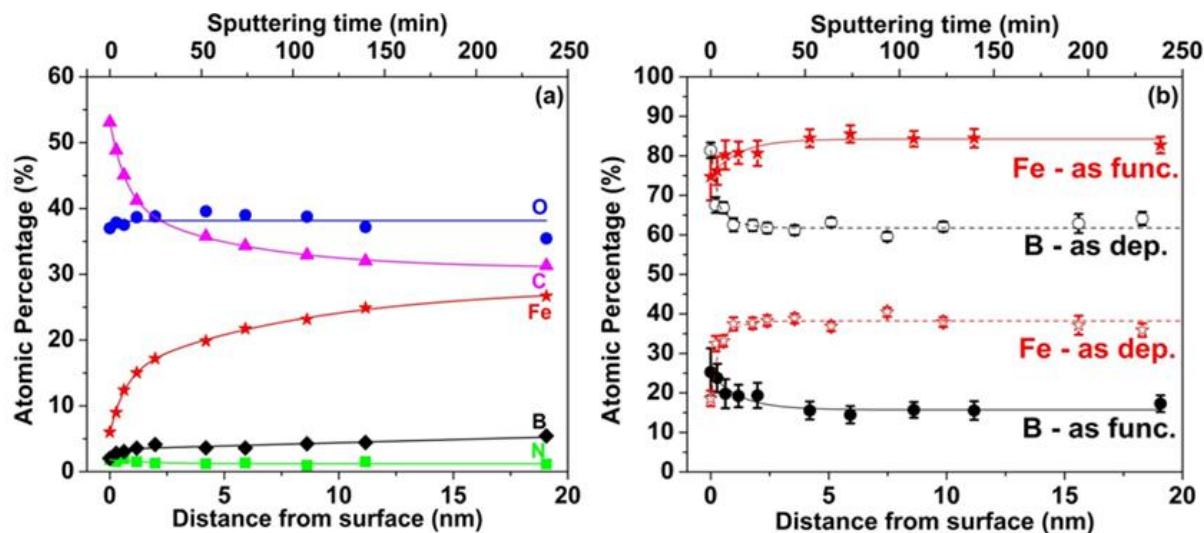


Figure 4: (a) Evolution of the atomic concentration of the most relevant elements from as functionalized FeB NPs, as a function of distance from the surface of the deposit. (b) Comparative evolution, between as deposited (red line) and as functionalized (black line) FeB NPs, of the atomic concentration of iron and boron as a function of distance from the surface of the deposit.

The deconvoluted high resolution spectra of Fe 2p after PEG attachment as a function of distance from surface are presented in figure 5a, while figure 5b display the corresponding evolution of the Fe states. Changes can be observed through the evolution of the shape of the spectra from 0 nm to 19.1 nm distance from surface. No significant binding energy shift was found regardless the distance from surface. Despite a rapid decrease at the very first depth stages, until 1.2 nm, the Fe^{3+} state is still dominant at almost all the thicknesses. In the opposite, the Fe^{2+} oxide concentration increases until 1.2 nm and then display an homogenous distribution along the whole depth. The most important change is related to the increasing non-oxidized Fe^0 state concentration. Although metallic iron is located closer to the surface than for the as deposited NPs, the evolution of the concentration with depth indicates a similar increasing trend. We note that such increase with depth is simultaneous with the decrease of Fe^{3+} state concentration. In a similar way as in the case of as deposited NPs, the depth profile indicates that iron atoms bond preferentially with oxygen³².

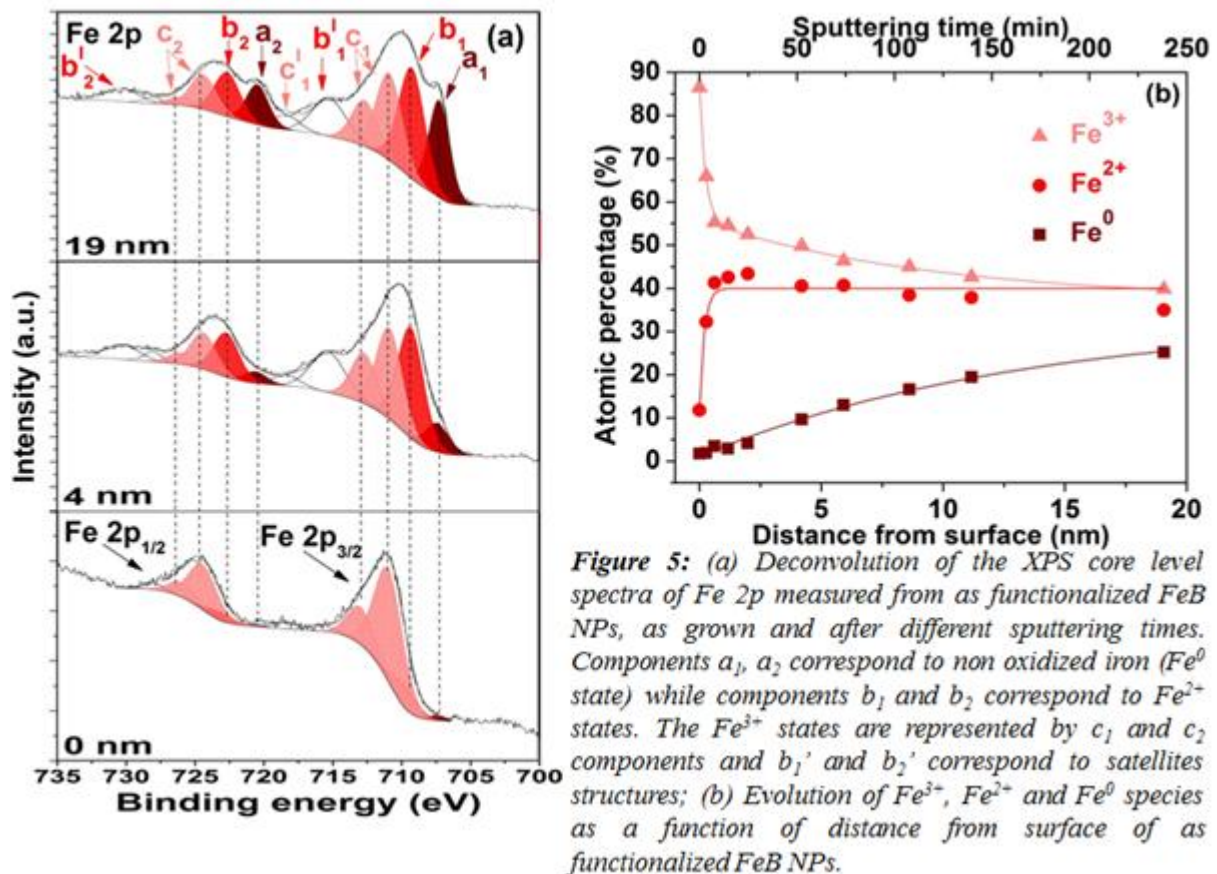


Figure 5: (a) Deconvolution of the XPS core level spectra of Fe 2p measured from as functionalized FeB NPs, as grown and after different sputtering times. Components a_1 , a_2 correspond to non oxidized iron (Fe^0 state) while components b_1 and b_2 correspond to Fe^{2+} states. The Fe^{3+} states are represented by c_1 and c_2 components and b_1' and b_2' correspond to satellites structures; (b) Evolution of Fe^{3+} , Fe^{2+} and Fe^0 species as a function of distance from surface of as functionalized FeB NPs.

The deconvolution of B 1s core levels shown in figure 6a were performed for as functionalized sample and upon different distance from surface in order to identify the chemical evolution in boron structure from surface to interior (figure 6b). As already discussed, B 1s core levels display a structure formed by two chemical groups, sub-stoichiometric B-O bonds and B-N bonds at the surface of as functionalized deposit. When comparing the boron structure which characterize the interior of as deposited sample (not shown here - see section III.3, Chapter III) where stoichiometric B_2O_3 oxide increases with increasing distance from surface, and the as functionalized sample, it is observed that there are no many differences between the surface and interior structures. Therefore no B_2O_3 contribution appears after 235 minutes of sputtering which correspond to 19.1 nm distance from surface. Also no significant binding energy shifts could be observed. From wide scans analysis shown in figure 4, a slightly increase of boron with depth was deduced. This is well emphasized also from the intensity of peaks in figure 6a. The profile evolution from figure 6b indicates that with increasing distance from surface the atomic concentration slightly decreases as a consequence of increase of the sub-stoichiometric boron oxide. This evidences that after functionalization the atomic concentration of sub-stoichiometric B-O groups is slightly higher in the interior than on the surface of NPs due to a higher solvent exposure

degree of the surface (during the functionalization process). The depth profiles of deconvoluted B 1s core levels indicate an almost homogenous dissolution of boron during the functionalization process. The high porosity of the deposit facilitates a high degree of dissolution of B-O groups from whole thicknesses.

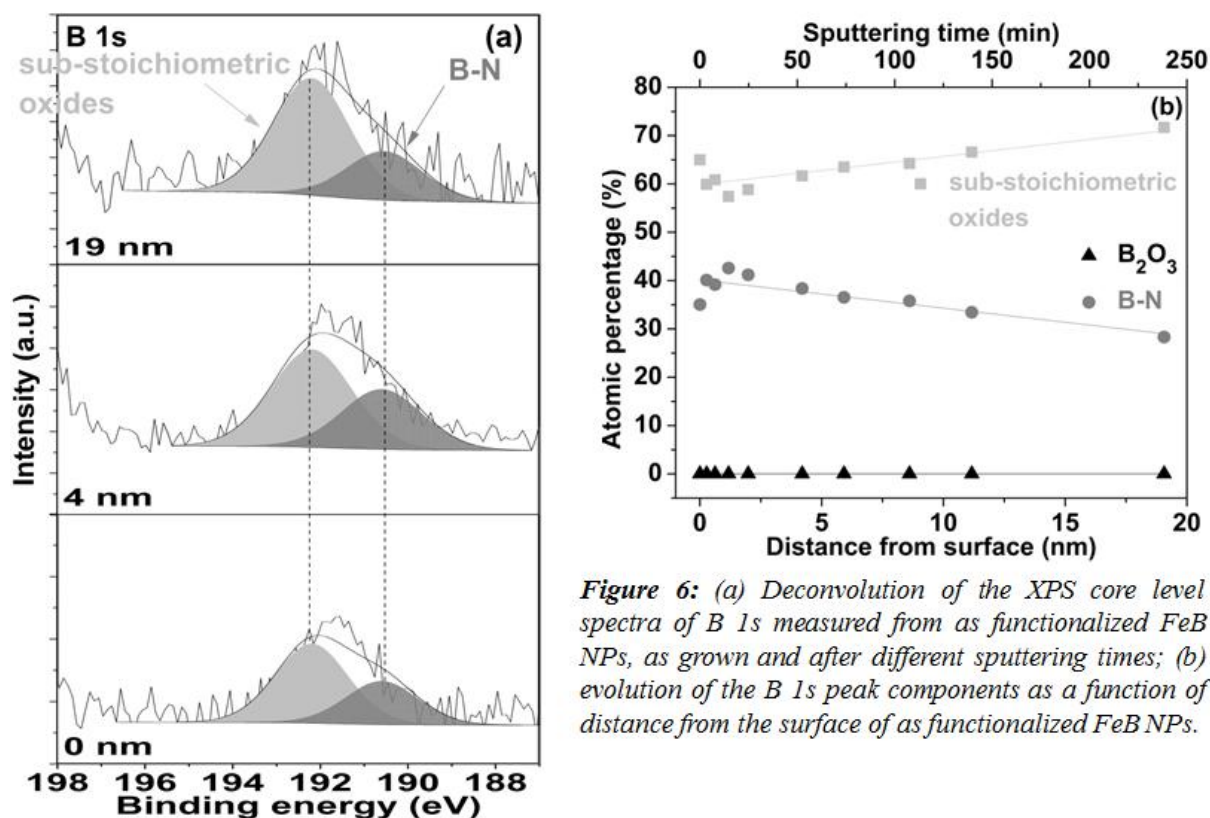


Figure 6: (a) Deconvolution of the XPS core level spectra of B 1s measured from as functionalized FeB NPs, as grown and after different sputtering times; (b) evolution of the B 1s peak components as a function of distance from the surface of as functionalized FeB NPs.

Although a multilayer deposit was used for functionalization, its high porosity also led to the dissolution of boron from the interior, not only from the surface of NPs located on the top of the deposit. This behavior has been proved by depth profile analysis on deconvoluted B 1s core levels, which emphasizes that before 19.1 nm distance from surface no significant changes related with the structure and the atomic concentrations of boron containing species were found.

The most important information evidenced from XPS analysis, regarding PEG attachment and the thickness of PEG layer from the surface of deposit, was obtained by depth profile analysis on deconvoluted O 1s core levels, displayed in figure 7a. The chemical evolution as a function of distance from surface is represented in figure 7b. No chemical shift is observed with increasing the distance from the surface in the case of O-C bonds and O-Fe bonds. The bands which correspond to OH/defective oxides and O-N bonds display only small variations of binding energy, close to surface value, in the ranges of 530.40 - 530.65 eV

and of 533.40 - 533.20 eV respectively. The stoichiometric O-Fe oxide was found in a considerable amount only at the surface and until to 0.62 nm distance from surface. Deeper in the layer, the O-Fe oxide concentration decrease dramatically to a minimum and constant value. However, it is well known from depth profile analysis of wide scans that iron has an increased concentration also inside of functionalized NPs. Therefore, the evolution of OH⁻/defective oxides found at all thicknesses, could also account for the increase of defective iron oxides with depth^{44,45,47}, and thus, explain this unusual behavior (similar as in the case of as deposited sample - see section III.3, Chapter III). The dominant concentration of O-C is closely linked to the existence of PEG at the surface of deposit. Due to a high porosity of as deposited sample, the evolution of this contribution proves that after functionalization, a high presence of PEG structures are bounded to NPs located in the interior of the deposit. From figure 7b, it is deduced that at distance from surface of 4.2 nm, O-C contribution stops to decrease and becomes constant. Taking into account this evolution, it inferred that PEG layer bounded at the top of the deposit has a thickness of around 4.2 nm. The concentration of O-N bonds display only a slightly decrease with distance from surface, having a low and almost constant distribution in NPs structure.

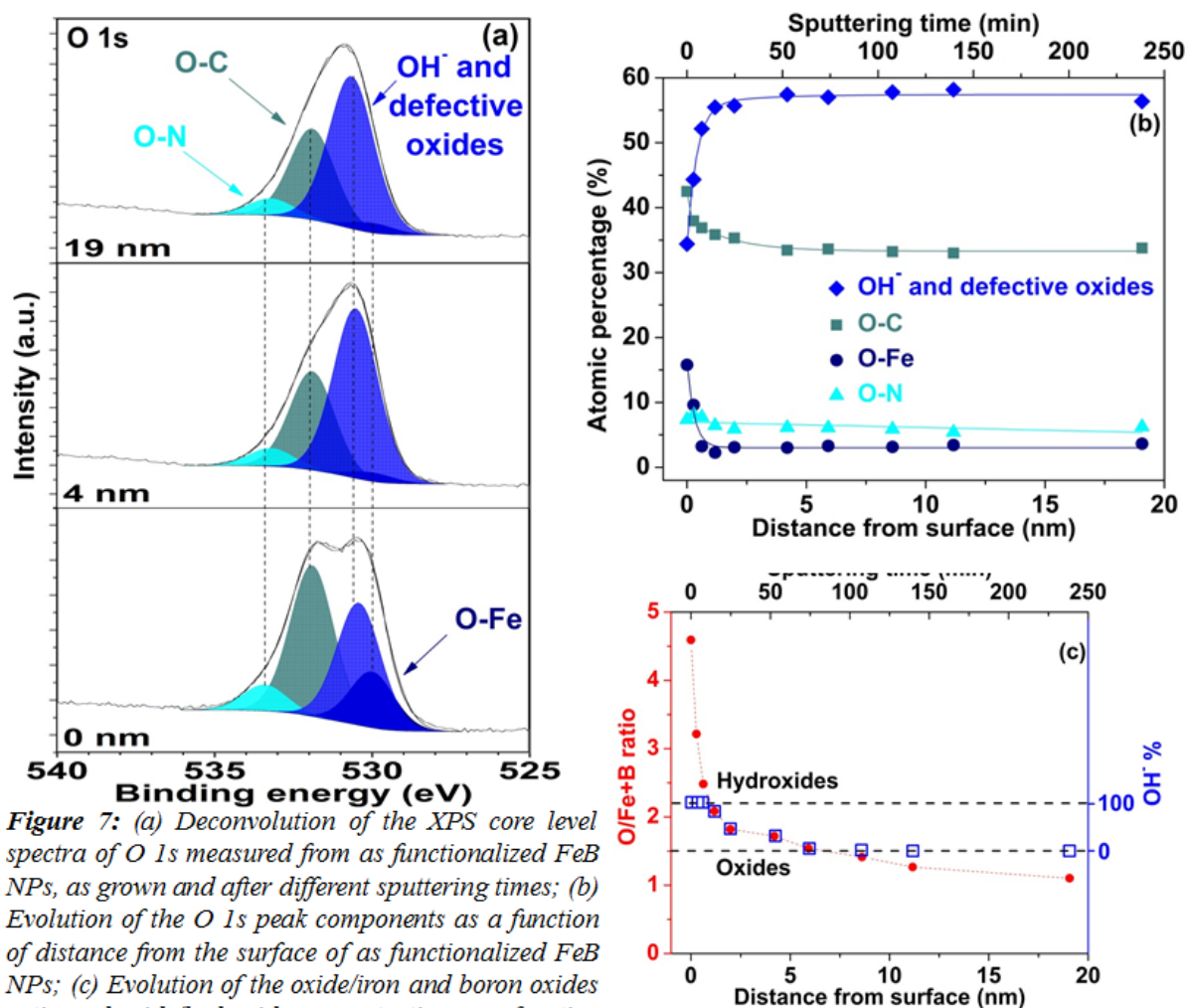


Figure 7: (a) Deconvolution of the XPS core level spectra of O 1s measured from as functionalized FeB NPs, as grown and after different sputtering times; (b) Evolution of the O 1s peak components as a function of distance from the surface of as functionalized FeB NPs; (c) Evolution of the oxide/iron and boron oxides ratio and oxide/hydroxide concentration as a function of distance from surface.

Therefore most of Fe and B are bonded to oxygen and the quantity of oxygen in form of O^{2-} being relatively small cannot explain the proportion of Fe^{2+} and Fe^{3+} . Considering the atomic percentages of O, Fe and B extracted from the wide scan (Figure 4), we calculated the $O/(Fe+B)$ ratio in order to determine the origin of the O 1s component located at 531.5 eV that could come from OH^- species or from oxygen vacancies in the oxide. The results are given in figure 7c. This ratio should be maximum 1.5 if all the oxygens exist in oxide state (Fe_2O_3 and B_2O_3 , respectively) and minimum 2.2 if all the oxygens are in hydroxide state (assuming that the quantity of Fe is four times higher than the B and that Fe_2O_3 and B_2O_3 were in the hydroxide form $Fe(OH)_2$ and $B(OH)_3$). Regarding our system, this ratio ranges from 4.6 on the surface and 1.1 at 19.1 nm distance from surface.

100% of the oxygen should be in hydroxide form if the ratio is 4.6. The $O/(Fe+B)$ ratio decreases very fast due to sputtering process in such a way that at 2.0 nm from the surface the ratio is 1.8. This means that the contribution of the hydroxide is below 45%.

Deeper in the layer, the ratio value is found below 1.5 after at 6 nm from the surface, highlighting that the hydroxide has no contribution. If we compare these calculations with the assignation of the components from the analysis of the O 1s core level peak (see figures 2d and 7), it is evident that the components at 530.40 eV and 530.00 eV cannot be attributed exclusively to the presence of hydroxides and oxides respectively. The analysis reveals that at the surface no evidence of oxides was found, the dominant structure being from iron and boron hydroxide. This indicates that, at the surface, the peak at 530.00 eV binding energy also correspond to an hydroxide state. On the opposite, deeper in the layer, the contribution of OH⁻ in O/Fe+B ratio is null, in contradiction with the assumption of the predominant peak at 530.40 to OH⁻ groups. Therefore deep in the layer, dominant contribution comes from oxides.

IV.1.2. Structural characterization: Raman

A comparative Raman analysis between as deposited and as functionalized FeB NPs was performed under an applied laser power of 0.14 mW (see figure 8). The reference Raman spectra for silicon wafer is also displayed (recorded with the laser power of 19.6 mW⁵⁹). We used such a low power of laser in order to preserve the NPs deposits and the PEG chains.

The higher amount of Fe-O and the lower amount of B-O proved by XPS analysis on as functionalized NPs are in good agreement with the intensity increase and the shift of the broad Raman structure from 625 cm⁻¹ and 688 cm⁻¹ after functionalization. Apart from the band which corresponds to Si-O asymmetric stretching vibration (at around 625 cm⁻¹), two other bands were found at higher wavenumbers, around 690 cm⁻¹ and 736 cm⁻¹ respectively. The related changes could be explained by the increase of γ -Fe₂O₃ groups and the chemical interaction between Fe-O/remained B-O groups with PEG chain. These wavenumber values close those reported in the literature⁶⁰ prove the formation of chemical bonds between Fe-O units located at the surface and PEG 400 structure. Also the relative intensity of these bands is higher than in FeB NPs, which is in agreement with the structural changes highlighted by XPS analysis (see figure 3).

The most important Raman information, which proves the presence of grafted PEG on the top of the deposit, is related with the growth at higher wavenumbers, in range of 1070-1800 cm⁻¹, of a broader and intense structure, suggesting a higher degree of interaction between polymer chains and surface of NPs deposit.

Therefore in literature, in the range of $1040\text{--}1160\text{ cm}^{-1}$, were found the bands representing C-O-C symmetric and asymmetric vibrations groups⁶¹⁻⁶⁴ and CH₂ symmetric vibration group⁶¹ from PEG chain. Furthermore the asymmetric, scissoring and wagging of CH₂ groups were found around $1220\text{--}1270\text{ cm}^{-1}$ ^{63,65-68}, 1350 cm^{-1} ^{61,66} and $1450\text{--}1510\text{ cm}^{-1}$ ^{61,63-66,68} respectively. The Raman spectra of as functionalized FeB NPs indicates more bands at 1145 cm^{-1} , 1268 cm^{-1} , 1356 cm^{-1} , 1456 cm^{-1} , 1489 cm^{-1} , corresponding to C-O-C symmetric and asymmetric vibrations/CH₂ symmetric vibration, asymmetric CH₂, scissoring CH₂ and wagging CH₂ (in case of last two bands) vibrations respectively.

There were evidenced two broad bands with the possible maxima at around 1323 cm^{-1} ^{69,70} and 1620 cm^{-1} ^{71,72}. Close to these two structures, in as deposited NPs is displayed the double phase structure, hematite and maghemite respectively. The increased intensity of both bands after functionalization is caused by the higher amount of Fe-O group near the surface level.

Another important result from Raman spectra regarding the PEG existence on top of the NPs deposit can be found at higher wavenumber values, in range of $2800\text{--}3100\text{ cm}^{-1}$ (see figure 8). The characteristic bands from that interval are represented by CH₂ symmetric and asymmetric stretching vibration^{64,65,67,68}. A wide structure, in the range $2846\text{--}3032\text{ cm}^{-1}$, appears in the

Raman spectra of as deposited (red spectra) and as functionalized NPs (blue spectra). Two different maxima are distinguishable at around 2880 cm^{-1} and 2940 cm^{-1} and are assigned to symmetric and asymmetric stretching vibrations respectively of CH groups. The higher intensity of this structure, which can be seen after PEG attachment (blue spectra), is an evidence of CH groups existence from PEG chain.

The Raman analysis have clearly demonstrated that ether groups of polyethylene (glycol) layer are present on the top of the NPs deposit⁷³.

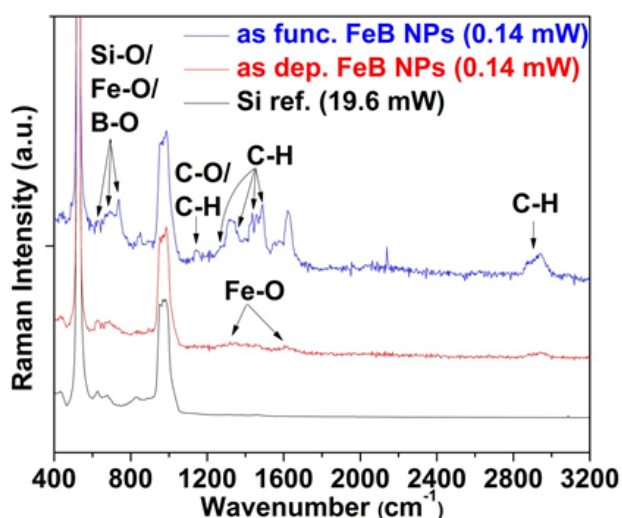


Figure 8: Comparative Raman spectra of Si substrate (black spectra), as deposited FeB NPs (red spectra) and as functionalized FeB NPs (blue spectra), recorded at a laser power of 0.14 mW.

IV.2 Dispersed and functionalized FeB NPs for in vitro MRI contrast agent applications

Considering the properties that characterize these NPs, highlighted in Chapter III, such as homogenous size distribution and spherical shape proved by AFM and TEM, superparamagnetic developed property as well as core shell structure proved by XPS and theoretical estimation of magnetic core size using Langevin and Triple fit, we considered to be appropriate for further applications as SPIO NPs. As will be pointed later, there is no doubt about the formation of ferrofluid solution even in the PEG uncoated FeB NPs.

For testing as MRI contrast agent it was important to use individual NPs which, when they are dispersed in an aqueous solution, have the ability to form a ferrofluid and no magnetic interaction arises between one to the other. Therefore a different way to functionalize was performed comparing with as functionalized FeB NPs, in order to reach a full coverage of the surface of NPs. Thus, the functionalization was carried out as we described in experimental section and we named these resulted entities as dispersed PEG-FeB NPs.

Even if we have already characterized the as deposited and as functionalized FeB NPs in terms of chemical structure, taking into account the different functionalization way used for obtaining PEG-FeB NPs, before to perform Magnetic Resonance Imaging analysis, were involved also UV-Vis analyses and Zeta Potential in order to assess the possibility of PEG embedded FeB NPs.

IV.2.1. Structural characterization: UV-Vis

The chemical and structural investigation performed on as functionalized FeB NPs surface, which was previously immersed into ultrapure deionized water during the functionalization process, indicate the dominant entities as being Fe-O and O-C groups and a small amount of sub-stoichiometric B-O groups. UV-Vis analysis investigated the changes in surface chemical structure due to PEG coating of dispersed NPs in aqueous solution (see figure 9). The attachment process of PEG polymer at the FeB NPs surface leads to some changes in UV-Vis spectra. The absorption spectra were recorded before and after PEG addition over the wavenumber range of 200 - 900 nm and a baseline correction corresponding to the absorption signal of a solvent was applied.

An important evidence for the PEG presence in the aqueous solution is the band that appears only in dispersed PEG FeB NPs at 230 nm. According with Sionkowska et al.⁷⁴ this

band is a signature of the presence of PEG. In their work they reported that the band of pure PEG should appear below 220 nm, but the tail of PEG absorption band could reach 400 nm. Hence the higher absorbance of dispersed PEG FeB NPs spectra could be understood by the contribution of PEG tail. A wide structure was seen in both spectra in the range 250-467 nm.

This structure could be attributed to the existence and possible overlap of more species within this wavenumbers range. Thus, one of the possible maximum appears at 312 nm. According to the literature, this maximum can be assigned to Fe^{2+} ^{75,76} and Fe^{3+} ions ^{75,77-80}, but also to B^{2+} ⁵⁵ bands. By showing the evolution of this band as a function of PEG attachment, in which case was found more prominent, could be evidenced the changes in iron oxide and

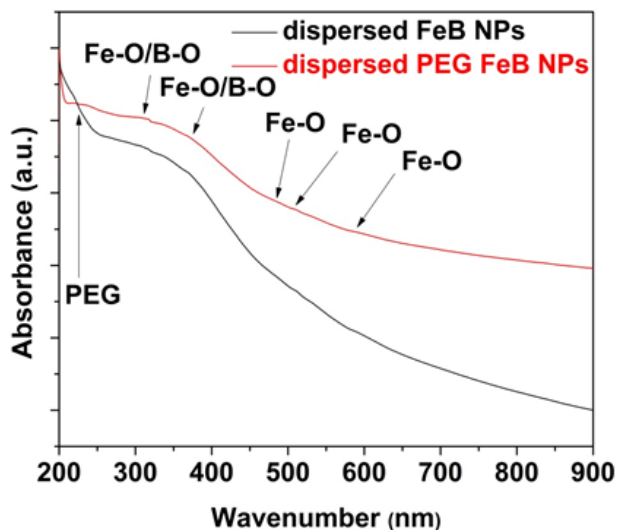


Figure 9: UV-Vis spectra of dispersed FeB NPs (black line) and dispersed PEG FeB NPs (red line).

boron oxide symmetry as a consequence of NPs-PEG chain interactions via oxygen atoms. The width of the structure suggest the presence of other bands. The lower wavenumber values contribution was attributed to the existence of tetrahedral Fe^{3+} oxides, which was found in previous studies at around 275 nm ⁸¹⁻⁸⁷. A larger intensity of this band, that appears regardless the functionalization process, could be an evidence of the distorted symmetry of tetrahedral Fe^{3+} species ^{75,87} or the simultaneously possible existence of Fe^{2+} ions ⁷⁵. The hardly visible band from 340 nm, which are visible in both spectra, may be assigned to octahedral Fe^{3+} oxides ^{75,83,84,87}. Other studies also reported that the Fe^{3+} oxides ions ^{75,78,87} and B^{2+} ⁵⁵ oxides should generate bands around 370 nm. Our spectra also present an absorption signal close to this value but individual entities are not distinguishable. At the higher extremity of this wide structure another possible band could appears at about 430 nm, representing the octahedral Fe^{3+} ions, as was reported by others ^{75,79,80,88-91}.

Beside these structures, other low intensity bands were observed in the absorption spectra at 484 nm, 508 nm and 589 nm wavenumber values, corresponding to Fe^{3+} ions ^{79,80,87}, octahedral Fe^{3+} oxides ^{83,84,87,92} and Fe-O groups located in FeO_4 structure ⁷⁵ respectively. Anyway, Rada et al. ⁷⁵ reported the possible existence of Fe^{2+} in the range 450-550 nm. It is important to mention that no changes were visible at these wavenumber values between both spectra.

IV.2.2. Surface charge characterization: Zeta Potential

The stability changes of NPs and coated NPs suspended in ultrapure deionized water was investigated by using zeta potential.

Variations in surface charge were measured using zeta potential analysis (see figure 10). These measurements were performed in order to study the PEG coverage of FeB NPs surface even after functionalization of fully dispersed NPs. An increase in zeta potential of NPs has been evidenced after PEG addition. In the case of dispersed FeB NPs, a negative charge of -28.23 mV with a standard deviation of 7.66 mV was observed in good agreement with a previous study on iron oxide NPs⁹³, while a positive potential of 9.31 mV with a standard deviation of 5.95 mV was determined for dispersed PEG FeB NPs. The existence of COOH groups at the FeB NPs surface was well correlated with the higher negatively charge of dispersed FeB NPs⁹¹.

Considering the previous work of Hu et al.⁶⁶ were the authors explained the fluctuation in zeta potential value as being dependent on surface neutralization of charge⁹⁵ or on the screening effect PEG coated NPs, we assume that the increase in zeta potential of PEG FeB NPs can be caused by a surface neutralization of the negative charges or the screening effect of FeB NPs PEG coating. This result reaches our expectations and change in terms of charge is an evidence of successful linking of PEG chains to NPs surface (dominated by iron oxide groups and a small concentration of boron oxide groups). Also of interest is that despite of the absence of ligand, the increase of zeta potential of dispersed PEG FeB NPs was higher, indicating that there is a higher density of PEG chains bonded at NPs surface.

This fact is in good agreement with the analysis performed on as functionalized NPs and with other studies, indicating the sterical colloidal stability of iron oxide NPs dispersed and functionalized with PEG^{93,96-98}. After PEG coverage of NPs the stability of dispersed NPs in aqueous solution was proved.

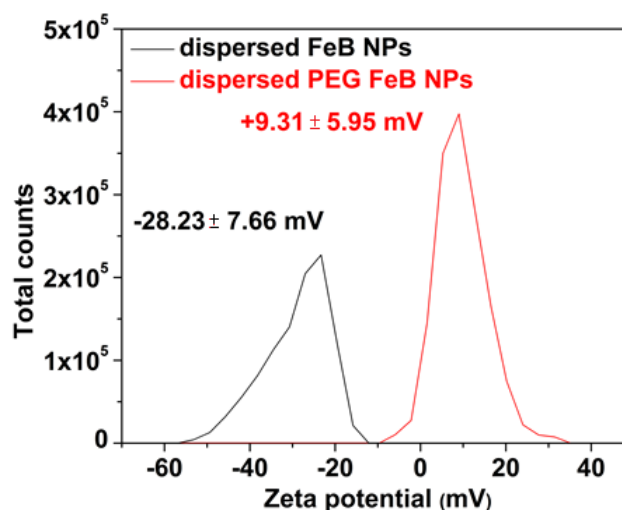


Figure 10: Zeta potential of dispersed FeB NPs (black line) and dispersed PEG FeB NPs (red line).

The presence of PEG chain on the NPs surface may induce a reduction in the surface toxicity level. Also, for *in vitro* analysis, it could play an important role in endocytosis and phagocytosis process as was related in other previous works⁹⁷. They found that as closer is zeta potential to zero values, the lower is endocytosis. On the opposite, at higher negative or positive charge, the phagocytosis increases^{97,99}.

IV.2.3. “*In vitro*” applications: MRI contrast agent

In this study our goal was to assess the effectiveness of the core/shell FeB NPs, coated with a biocompatible polymer layer, in T_2 signal reduction via *in vitro* MRI analysis. The contrast dependence on the NPs concentration, NPs functionalization together with the NPs stability in time was also evaluated. NPs dispersed in aqueous solution relative to blank water (as control) were used for MRI analysis.

IV.2.3.1. Contrast enhancement as a function of NPs concentration

Three different images corresponding to the three concentrations of NPs, 0.15 mM, 0.30 mM and 0.44 mM in aqueous solution, were recorded to assess the dependence of contrast on NPs concentration (see figure 11a).

The possible use of superparamagnetic FeB NPs as contrast agent was evaluated by monitoring the changes in the T_2 transverse relaxation time of water protons¹⁰⁰ in the presence of different concentrations of NPs.

The decreasing T_2 relaxation time has been determined for each NPs concentration and compared to the T_2 value corresponding to ultrapure deionized water. The comparative analysis as a function of NPs concentrations shows an attenuation trend of the T_2 signal with increasing the nanoparticles concentration. Thus, the sample with lower NPs concentration evidence a 23.1% reduction in T_2 signal relative to that of the control (see Table 1). Increased attenuation was found for the samples with higher NPs concentration, the nanoparticles reducing the T_2 -weighted signal by 46.9% and 49.0% for the 0.30 mM and 0.44 mM respectively (see Table 1). These

NPs concentration (mM)	T_2 (s)	R_2 (s^{-1})	r_2 ($s^{-1}mM^{-1}$)
0.00	0.143	6.99	-
0.15	0.110	9.09	13.99
0.30	0.076	13.16	20.55
0.44	0.073	13.70	15.24

Table 1: The obtained values of relaxation time, relaxation rate and relaxivity as a function of FeB NPs concentration.

values were found to be in good correlation with other values reported in literature^{100,101,102} that indicates the increase of MRI signal with T_2 attenuation (which will lead to a much darker image).

This behavior suggests a T_2 contrast enhancement dependent on concentration. An almost saturation state in term of contrast may be achieved by increasing the NPs concentration due to the fact that the distance between neighboring dispersed entities reaches a minimum.

The relaxation rates were also highlighted here as a function of dispersed FeB NPs concentration, evidencing a continuously enhancement of R_2 by increasing the NPs concentration (see figure 11b, Table 1).

To clearly emphasize the potential use of NPs as contrast agent, the transverse relaxivity r_2 was also determined for all concentrations. The evolution of this parameter could indicate the possible use of NPs as MRI contrast agent¹².

As expected, changes in r_2 relaxivity appear when increasing the concentration of the NPs. The r_2 values calculated for each concentration (0.15 mM, 0.30 mM and 0.44 mM) were $13.99 \text{ mM}^{-1}\text{s}^{-1}$, $20.55 \text{ mM}^{-1}\text{s}^{-1}$ and $15.24 \text{ mM}^{-1}\text{s}^{-1}$ respectively (see Table 1). Even though the R_2 relaxation rate has a continuous increase with concentration (see figure 11b), we observe a r_2 relaxivity decrease for the sample with the highest concentration as compared with the others. A similar behavior was also discussed in a previous work¹⁰³ where it was stated that a higher NPs concentration with a higher relaxation rate can rich similar contrast with a lower NPs concentration and a smaller relaxation rate. A dependency of concentration was related with the evolution of contrast and an inversion point was well highlighted, where the increase in NPs density, dispersed in aqueous solution, do not improve the efficiency as contrast agent regardless the increasing trend of R_2 relaxation rate. The lack of linear R_2 increase may be explained by the decrease of the inter-particle distance as a consequence of partial NPs aggregation under the applied magnetic field. This fact indicates that, in order to avoid the inter-particles aggregation, the optimal FeB NPs concentration, for applications as MRI contrast agent, should be around 0.30 mM.

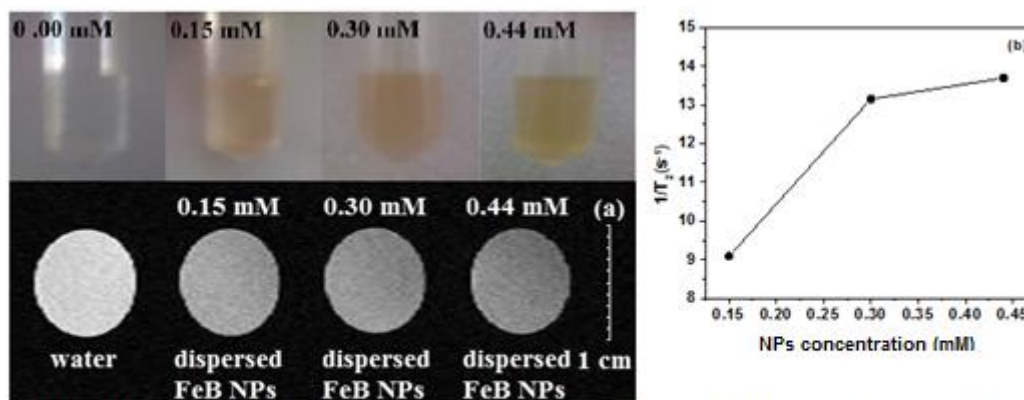


Figure 11: (a) T_2 -weighted magnetic resonance imaging at 7 T comparing the T_2 contrast (darkening) from ultrapure deionized water and dispersed FeB NPs with three different concentrations, 0.15 mM, 0.30 mM and 0.44 mM.; (b) The relaxation rate R_2 in relation to the NPs concentrations of dispersed FeBNPs.

IV.2.3.2. Coating influence on contrast enhancement and colloidal stability

The next step was to assess the differences, in terms of contrast and over time stability, between aqueous dispersed FeB NPs and PEG coated FeB NPs considering the concentration of 0.30 mM in both cases (see figure 12b). The T_2 relaxation times were determined for both FeB and PEG FeB NPs and compared with the T_2 values recorded for ultrapure deionized water. T_2 -weighted MR images have been recorded shortly after the functionalization procedure and 2 hours later (see figures 12a,b). Even though the same NPs concentration was used, a slightly lower T_2 signal reduction was reported for the PEG FeB NPs (see figure 12a). The reduction of T_2 signal of the PEG functionalized NPs was found to be 39.9 % relative to that of non-functionalized FeB-NPs (61.6 %). This is a normal behavior considering that the mean size of the PEG FeB NPs (and thus, the surface area) and the molecular weight is increased compared to uncoated dispersed NPs¹⁰⁰, due to the PEG chain contribution at NPs surface and thus, the distance between neighboring magnetic cores increases. Thus, the r_2 relaxivity was found to be much higher in the case of uncoated NPs, being around $35.55 \text{ mM}^{-1}\text{s}^{-1}$ while the one of coated NPs was found to be at about $14.69 \text{ mM}^{-1}\text{s}^{-1}$ (see figure 12b). This reduction was linked with the decrease of superparamagnetic signal¹⁰⁰.

The stability over time was well proved by the MRI measurements registered after 2 hours. The T_2 alterations for dispersed NPs and dispersed PEG NPs were found to be 59.6% and 37.6% which evidences that no important change occurs over time in terms of T_2 relaxation time.

A very small decrease of r_2 relaxivity was observed after 2 hours of immersion for both FeB NPs and PEG FeB NPs samples. Relaxivity values decreased by $1.97 \text{ mM}^{-1}\text{s}^{-1}$ and $1.18 \text{ mM}^{-1}\text{s}^{-1}$ respectively, relative to those initially recorded which represent 7.7% and 8.0% respectively. The small change in relaxivity over time could be attributed to the existence of a weak ferromagnetism as evidenced by SQUID measurements performed on as deposited NPs (see section III.4, Chapter III), and caused probably by the smaller size distribution of the NPs evidenced by AFM analysis also recorded on as deposited FeB NPs (data not shown here). These NPs could aggregate faster under the influence of a magnetic field due to a higher remanent magnetization. These findings reinforce the idea that no important changes in terms of colloidal stability occur as a function of time after dispersion in the aqueous solution.

From the above analysis it is deduced that the presence of PEG layer on the top of FeB NPs affects the reflexivity which indicates a lower efficiency as contrast agent as compared to bare FeB NPs. Even if the uncoated NPs develop a higher reflexivity, the PEG attachment represents a compromise solution in terms of NPs biocompatibility^{10-12,15-17,104-106}.

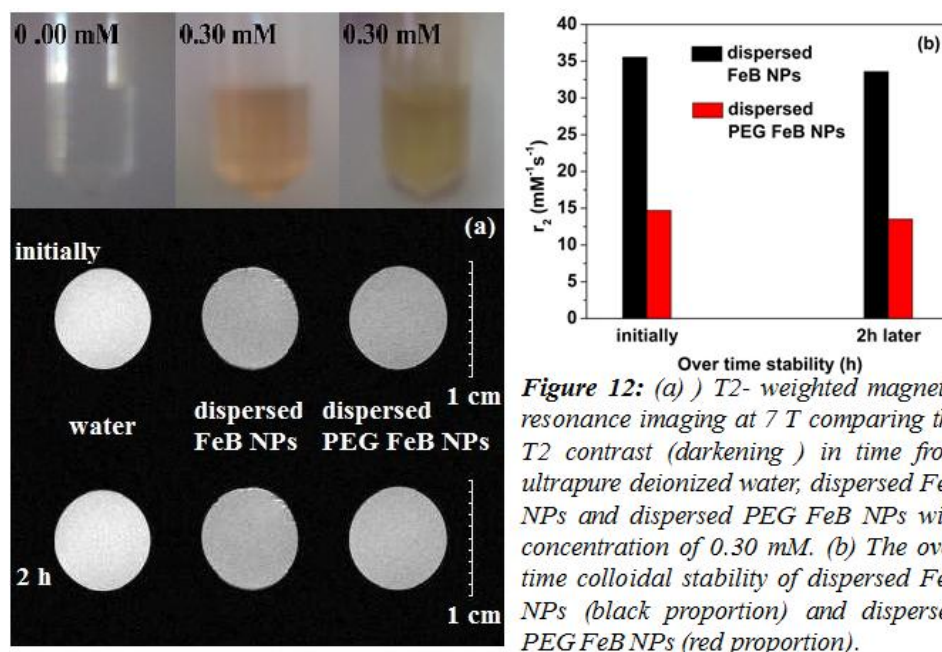


Figure 12: (a) T_2 - weighted magnetic resonance imaging at 7 T comparing the T_2 contrast (darkening) in time from ultrapure deionized water, dispersed FeB NPs and dispersed PEG FeB NPs with concentration of 0.30 mM. (b) The over time colloidal stability of dispersed FeB NPs (black proportion) and dispersed PEG FeB NPs (red proportion).

Conclusions

The initial of the present work was to fabricate and characterize superparamagnetic and amorphous FeB nanoparticles with diameter in range of 10-20 nm, which can be used in medicine as for example MRI contrast agent and also in technological applications field.

AFM and TEM characterizations have demonstrated the spherical shape of the fabricated nanoparticles. TEM measurements have also revealed the amorphous nature of the nanoparticles deposit.

The XPS elemental composition in depth was characterized by an exchange composition from surface to core with an increase of Fe/B ratio (from 0.29 to 0.56, and after a longer Ar⁺ ion bombardment time, corresponding to 1.8 nm of depth, the ratio becomes quite constant with slight variations) and oxidation level. A core-shell structure characterizes FeB nanoparticles with an iron and a shell of iron and boron mixture. The nanoparticles present non ferromagnetic behavior at room temperature, because iron atoms are insulated in a boron oxide matrix. AFM and TEM characterization revealed a very large size distribution of FeB nanoparticles. The relatively small superparamagnetic size deduced from SQUID measurements can be understand by the presence of a very thick oxide shell with a wide range of thickness which also indicates a strong influence of the oxygen on the resulting properties of the nanoparticles.

The reduced effective magnetic size determined from Langevin Fit and Triple Fit together with the presence of an oxide shell with different thickness surrounding the magnetic entities are in contradiction with the narrow distribution of blocking temperature. We can explain that strange behavior by the fact that the shell structure is nonmagnetic and there are no influences in the magnetic response of the nanoparticles due to the different thickness of oxide shell.

In order to avoid the earlier clearance from biological media, after their growth, the NPs were coated with polyethylene-glycol (PEG).

Two different coating techniques were performed. First, for a better highlighting of PEG attachment and of changes in structural and chemical properties, the NPs deposit was functionalized directly on SiO_x wafer.

XPS deposit analysis of between wide scans and high resolution spectra of uncoated and coated NPs revealed important changes in surface chemical structure characterized by a decrease in boron amount after functionalization, from 81.4% to 25.3%, while the iron amount increases from 19.6% to 74.7%. The dissolution of an important boron amount after NPs deposit immersion was emphasized by UV-Vis analysis performed on the aqueous solution used for functionalization that indicated the presence of boron. The PEG attachment to the surface of NPs deposit was well identified by the increased amount of oxygen and carbon groups due to the additional contribution of CH₂-O units originated from PEG chains. The XPS data were also sustained by FTIR and Raman structural analyses which highlighted the presence of ether groups from polyethylene (glycol) layer on coated NPs.

The changes in chemical groups, between surface and the interior of functionalized NPs, were investigated in the range of 0 - 19.1 nm distances from surface. Despite the decrease of boron concentration after PEG attachment, the evolution with depth is similar as in the case of as deposited samples, with an increase of the iron amount from surface to interior, as a consequence of boron decrease. The chemical evolution with depth indicates a slightly higher oxidation at very first depth stages, until 1.2 nm distance from surface. In a similar way as in case of the as deposited NPs, the depth profile showed that iron atoms bond preferentially with oxygen. Metallic iron appears much closer to the NPs surface after functionalization. The high porosity of the deposit led to the dissolution of boron from the interior. Comparing with the boron structures that characterize the interior of as deposited NPs, no important differences between 0 nm and 19.1 nm could be observed for as functionalized NPs, with an almost homogenous distribution of sub-stoichiometric B-O groups regardless the depth. The nitrogen concentration also displayed an almost homogenous distribution along the whole depth. From the evolution with distance from surface of O-C groups, originating from PEG structure, the thickness of PEG layer bounded from the top of the deposit was found to be approximately 4.2 nm. Anyway, a substantial and constant amount of this structure was found also in the interior of the deposit, being caused by the high porosity of the deposit. While the oxygen from the surface was found in hydroxide state, a transition to oxide state was observed and after 6 nm distance from surface, no contribution of hydroxide was found.

In the second way, for investigating the contrast enhancement, the NPs were first separated from the substrate and then coated with polyethylene-glycol. The UV-Vis and Zeta Potential measurements on dispersed PEG FeB NPs evidenced, in good agreement with XPS,

Raman and IR measurements on as functionalized NPs, the chemical interactions between the surface of NPs and PEG chains.

Three different concentrations of 0.15 mM, 0.30 mM and 0.44 mM were used to investigate the changes in contrast as a function of NPs concentration. The lack of linear R_2 increase may be explained by the decrease of the inter-particle distance as a consequence of partial NPs aggregation under the applied magnetic field. To prevent the inter-particles aggregation, the optimal FeB NPs concentration, for applications as MRI contrast agent, should be around 0.30 mM with a relaxivity of $20.55 \text{ mM}^{-1}\text{s}^{-1}$.

In order to study the effect in terms of contrast after PEG coating, the NPs concentration of 0.30 mM was investigated before and after functionalization. A decrease of superparamagnetic signal was relieved in PEG coated NPs, caused by the diminution of r_2 relaxivity, which was found to be much lower ($14.69 \text{ mM}^{-1}\text{s}^{-1}$) as compared with the one of uncoated NPs ($35.55 \text{ mM}^{-1}\text{s}^{-1}$). The PEG coated NPs showed a lower efficiency as contrast agent. Anyway, its attachment represents a compromise solution in terms of NPs biocompatibility. No important changes in terms of colloidal stability were identified as a function of time after dispersion in the aqueous solution.

As already mentioned, the *in vitro* MRI analysis was carried out under an applied magnetic field of 7 T. This fact is important since clinical MRI is evolving also to higher fields for the investigation of nanoparticles as contrast agents¹².

The idea of using NPs based on iron as MRI contrast agent was already discussed^{5,107}. It is well known that the size of NPs represents an important parameter regarding the relaxivity evolution. The smaller are the NPs the lower is the relaxivity^{16,100}, in well correlation with the saturation magnetization, which decreases with the magnetic size¹⁰⁸. In particular, the iron oxide NPs of 4 nm show a relaxivity at around $75 \text{ mM}^{-1}\text{s}^{-1}$ ¹⁶. Taking into account that the superparamagnetic size of FeB NPs was found to be 2.9 nm (see section III.4, Chapter III), the relaxivity value is close to the one from literature. A similar study on FeB NPs was found¹⁰⁹. Comparing with this, where the r_2 relaxivity was obtained to be $9.96 \text{ mM}^{-1}\text{s}^{-1}$, the FeB NPs from our study showed a higher r_2 relaxivity and thus a powerful T_2 contrast enhancement. In conclusion, from the above analysis, the response of superparamagnetic FeB NPs and PEG FeB NPs as MRI contrast agent is promising for further *in vivo* study.

References

- ¹ M. L. Liu, H. L. Zhou, Y. R. Chen, Y. Q. Jia, *Materials Chemistry and Physics*, **89**, 289 (2005).
- ² Y. Fan, Z. Hu, J. Shen, Q. Yan, Y. Chen, *J. Mater. Sci. Lett.* **12**, 596 (1993).
- ³ H. Wang et al., *Appl. Catal. A*, **129**, L143 (1995).
- ⁴ I. Narita, T. Oku, H. Tokoro and K. Suganuma, *Journal of Electron Microscopy*, **55** (3), 123 (2006).
- ⁵ L. Calucci, G. Ciofani, D. De Marchi, C. Forte, A. Menciasci, L. Menichetti, V. Positano, *J. Phys. Chem. Lett.* **1**, 2561–2565 (2010).
- ⁶ J. Bansmann, S. H. Baker, C. Binns, J. A. Blackman, J. P. Bucher, J. Dorantes-Davila, V. Dupuis, L. Favre, D. Kechrakos, A. Kleibert, K. H. Meiwes-Broer, G. M. Pastor, A. Perez, O. Toulemonde, K. N. Trohidou, J. Tuaille, Y. Xie, *Surf. Sci. Rep.* **56**, 189 (2005).
- ⁷ M. Diaz, E. Roman, L. Martinez, R. Fermento, M. M. Ruano, M. Garcia-Hernandez, A. Cebollada, D. Llamosa P, C. Ballesteros, G. Armelles, Y. Huttel, *J. Nanopart. Res.* **13**, 5321 (2011).
- ⁸ L. Martínez, M. Díaz, E. Román, M. Ruano, D. Llamosa P., Y. Huttel, *Langmuir*, **28**, 11241 (2012).
- ⁹ Oxford Applied Research, <http://www.oaresearch.co.uk>.
- ¹⁰ C. Corot, P. Robert, J. M. Idée, M. Port, *Advanced Drug Delivery Reviews*, **58**, 1471–1504 (2006).
- ¹¹ C. Barrera, A. P. Herrera, C. Rinaldi, *Journal of Colloid and Interface Science*, **329**, 107–113 (2009).
- ¹² A. Carvalho, M. Clara Gonçalves, M. B. F. Martins, D. Meixedo, G. Feio, *Magnetic Resonance Imaging*, **31**, Issue 4, 610–612 (2013).
- ¹³ Y. Zhang, J. Zhang, *Journal of Colloid and Interface Science*, **283**, 352–357 (2005).
- ¹⁴ S. A. Koch et. al, *Appl. Phys. Lett.* **84**, 26 (2004).
- ¹⁵ J. E. Rosen, L. Chan, D. –B. Shieh, DDS, DMSc, Frank X. Gu, PhD, *Nanomedicine: Nanotechnology, Biology, and Medicine* (2011).
- ¹⁶ M. A. Hahn, A. K. Singh, P. Sharma, S. C. Brown, B. M. Moudgil, *Anal Bioanal Chem.* **399**, 3–27 (2011).
- ¹⁷ C. C. Berry and A. S. G. Curtis, *J. Phys. D: Appl. Phys.* **36**, R198 (2003).
- ¹⁸ K. O’Grady, A. Bradbury, *J. Magn. Mater.* **39**, 91 (1983).
- ¹⁹ M. M. Ruano, M. Díaz, L. Martínez, E. Navarro, E. Román, M. García-Hernandez, A. Espinosa, C. Ballesteros, R. Fermento, Y. Huttel, *Phys. Chem. Chem. Phys.* **15**, 316 (2013).
- ²⁰ I. Fernandez-Martinez, M. S. Martin-Gonzalez, R. Gonzalez-Arrabal, R. Alvarez-Sancheza, F. Brionesa, J. L. Costa-Kramer, *Journal of Magnetism and Magnetic Materials* **320**, 68–75 (2008).
- ²¹ M. S. Martin-Gonzalez, Y. Huttel, A. Cebollada, G. Armelles, F. Briones, *Surf. Sci.* **571**, 63 (2004).
- ²² O. Ponta, C. Gruian, E. Vanea, B. Oprea, H.J. Steinhoff, S. Simon, *Journal of Molecular Structure*, 1044, 2-9 (2013);
- ²³ K. Kumari, S. Ram, R. K. Kotnala, *Materials Chemistry and Physics*, **129**, 1020 (2011).
- ²⁴ F. Stobiecki, S. Schwarzl, T. Stobiecki and H. Hoffmann, *Colloque C8, suppliment au n^o8, Tome 41, page C8-171* (1980).
- ²⁵ A. Essafti, A. Abouelaoualim, J. L. G. Fierro, E. Ech-chamikh, *Thin Solid Films*, **517**, 4281 (2009).
- ²⁶ G. D. Khattak, M. A. Salim, L. E. Wenger, A. H. Gilani, *Journal of Non-Crystalline Solids*, **244**, 128 (1999).
- ²⁷ P. C. J. Graat, M. A. J. Somers, *Surf. Interf. Anal.* **26** (11), 773 (1998).
- ²⁸ P. C. J. Graat, M. A. J. Somers, *Appl. Surf. Sci.* **101**, 36 (1996).

- ²⁹ A. P. Grosvenor, B. A. Kobe, M. C. Biesinger, N. S. McIntyre, *Surface and Interface Analysis*, **36**, 1564 (2004).
- ³⁰ S. J. Roosendaal, I. A. M. E. Giebels, A. M. Vredenberg, F. H. P. M. Habraken, *Surf. Interf. Anal.* **26** (10), 758 (1998).
- ³¹ K. Wandelt, *Surf. Sci. Rep.* **2**, 75 (1982);
- ³² M. Grafouté, C. Petitjean, C. Rousselot, J. F. Pierson, J. M. Grenèche, *Scr. Mater.* **56**, 153 (2007).
- ³³ C. D. Wagner, W. M. Riggs, L. E. Davis, J. F. Moulder, in: G.E. Muilenberg (Ed.), Perkin-Elmer Co., Minnesota, 1979.
- ³⁴ D. Schild, S. Ulrich, J. Ye, M. Stüber, *Solid State Sciences*, **12**, 1903-1906 (2010).
- ³⁵ C. L. Perkins, M. Trenary, T. Tanaka, S. Otani, *Surface Science*, **423**, 222–228 (1999).
- ³⁶ C. W. Ong, H. Huang, *Journal of Applied Physics*, **95**, 7 (2004).
- ³⁷ Y. Wang, M. Trenary, *Chem. Mater.* **5**, 199-205 (1993).
- ³⁸ B. Van Devenner, J. P. L. Perez, S. L. Anderson, *J. Mater. Res.* **24**, 11 (2009).
- ³⁹ O. M. Moon, B. C. Kang, S. B. Lee, J. H. Boo, *Thin Solid Films*, **464–465**, 164–169 (2004).
- ⁴⁰ Y. P. Xie, G. Liu, G. Q. Lub, H. -M. Cheng, *Nanoscale*, **4**, 1267 (2012).
- ⁴¹ J. F. Pierson, C. Rousselot, *Surf. Coat. Technol.* **180–181**, 44 (2004).
- ⁴² G. Bhargava, I. Gouzman, C. M. Chun, T. A. Ramanarayanan, S. L. Bernasek, *Applied Surface Science*, **253**, 4322–4329 (2007).
- ⁴³ A. Ennaoui, S. Fiechter, W. Jaegermann, H. Tributsch, *Journal of the Electrochemical Society*, **133**, 97-106 (1986).
- ⁴⁴ S. Karthe, R. Szargan, E. Suoninen, *Applied Surface Science*, **72**, 157-170 (1993).
- ⁴⁵ K. Sasaki, *Geochimica et Cosmochimica Acta*, **58**, 4649-4655 (1994).
- ⁴⁶ C. M. Eggleston, J. J. Ehrhardt, W. Stumm, *American Mineralogist*, **81**, 1036-105 (1996).
- ⁴⁷ D. J. Joyner, D. M. Hercules, *J. Chem. Phys.* **72**, 1095 (1980).
- ⁴⁸ B. Oprea, T. Radu, S. Simon, *Journal of Non-Crystalline Solids*, **379**, 35–39 (2013).
- ⁴⁹ J. F. Moulder, W. F. Stickle, P. E. Sobol, K. D. Bomben, *Physical Electronics, Inc.* (1995).
- ⁵⁰ C. P. Bean, J. D. Livingston, *J. Appl. Phys.* **30**, 120 (1959).
- ⁵¹ Y. Shiratsuchi, M. Yamamoto, Y. Endo, D. Li, S. D. Bader, *J. Appl. Phys.* **94**, 767 (2003).
- ⁵² A. Tamion, M. Hillenkamp, F. Tournus, E. Bonet, V. Dupuis, *Appl. Phys. Lett.* **95**, 062503 (2009).
- ⁵³ J. Carvell, E. Ayieta, A. Gavrin, R. Cheng, V. R. Shahand, P. Sokol, *Journal of Applied Physics*, **107**, 103913 (2010).
- ⁵⁴ M. S. Martin-Gonzalez, Y. Huttel, A. Cebollada, G. Armelles, F. Briones, *Surf. Sci.* **571**, 63 (2004).
- ⁵⁵ Q. Ling, J. Sun, Q. Zhou, Q. Zhao, H. Ren, *Journal of Photochemistry and Photobiology A: Chemistry*, **200**, 141–147 (2008).
- ⁵⁶ J. F. Moulder, W. F. Stickle, P. E. Sobol, K. D. Bomben, *Handbook of X-ray Photoelectron Spectroscopy*, Perkin-Elmer Corporation, Physical Electronics Division, Eden Prairie (1992).
- ⁵⁷ Y. Fu, H. Du, S. Zhang, W. Huang, *Materials Science and Engineering A*, **403**, 25–31 (2005).
- ⁵⁸ V. Datsyuk, M. Kalyva, K. Papagelis, J. Parthenios, D. Tasis, A. Siokou, I. Kallitsis, C. Galiotis, *CARBON*, **46**, 833–840 (2008).

- ⁵⁹ P. Borowicz, M. Latek, W. Rzdokiewicz, A. Łaszcz, A. Czerwinski, J. Ratajczak, *Adv. Nat. Sci.: Nanosci. Nanotechnol.* **3** (2012).
- ⁶⁰ Y. GOURBEYRE, E. GUILMINOT, F. DALARD, *JOURNAL OF MATERIALS SCIENCE*, **38**, 1307 – 1313 (2003).
- ⁶¹ H. Y. Jung, R. K. Gupta, E. O. Oh, Y. H. Kim, C. M. Whang, *Journal of Non-Crystalline Solids*, **351**, 372–379 (2005).
- ⁶² B. Bozzini, L. D'Urzo, C. Mele, V. Romanello, *J. Mater. Sci.: Mater. Electron*, **17**, 915 (2006).
- ⁶³ V. Califano, F. Bloisi, L. R. M. Vicari, P. Colombi, E. Bontempi, L. E. Depero, *Applied Surface Science*, **254**, Issue 22, 7143–7148 (2008).
- ⁶⁴ E. Tamariz, A. C. A. Wan, Y. S. Pek, M. Giordano, G. Hernandez-Padron, A. Varela-Echavarria, I. Velasco, V. M. Castano, *J Mater Sci: Mater Med.* **22**, 2097–2109 (2011).
- ⁶⁵ N. B. Colthup, L. H. Daly, S. E. Wiberley, *Introduction to Infrared and Raman Spectroscopy* (Academic Press, Boston) (1990).
- ⁶⁶ L. Hu, D. Hach, D. Chaumont, C. -H. Brachais, J. -P. Couvercelle, A. Percheron, *J Sol-Gel Sci Technol*, **49**, 277–284 (2009).
- ⁶⁷ S. Gunasekaran, E. Sailatha, S. Seshadri, S. Kumaresan, *Indian Journal of Pure & Applied Physics*, **47**, 12-18 (2009).
- ⁶⁸ L. D'Urzo, B. Bozzini, *J Mater Sci: Mater Electron*, **20**, 217–222 (2009).
- ⁶⁹ M. H. Sousa, F. A. Tourinho, J. C. Rubim, **31**, Issue 3, 185-191 (2000).
- ⁷⁰ X. Bo, G. Li, X. Qiu, Y. Xue, L. Li, *Journal of Solid State Chemistry*, **180**, Issue 3, 1038–1044 (2007).
- ⁷¹ L. Slavov, M. V. Abrashev, T. Merodiiska, C. Gelev, R. E. Vandenberghe, I. Markova-Deneva, I. Nedkov, *Journal of Magnetism and Magnetic Materials*, **322**, Issue 14, 1904–1911 (2010).
- ⁷² C. Guo, Y. Hu, H. Qian, J. Ning, S. Xu, *Materials Characterization*, **62**, Issue 1, 148–151 (2011).
- ⁷³ T. -W. Lin, C. G. Salzmann, L. -D. Shao, C. -H. Yu, M. L. H. Green, *Carbon*, **47**, Issue 6, 1415–1420 (2009).
- ⁷⁴ Sionkowska, *Polymer Degradation and Stability*, **91**, 305-312 (2006).
- ⁷⁵ S. Rada, A. Dehelean, E. Culea, *J Mol Model*, **17**, 2103–2111 (2011).
- ⁷⁶ E. J. Friebele, D. R. Ullmann, N. J. Kreidl, *American Ceramic Society*, Westerville, 205 (1991).
- ⁷⁷ Y. Tanabe, S. Sugano, *J. Phys. Soc. Jpn.* **9**, 753 (1954).
- ⁷⁸ D. M. Sherman, T. D. Waits, *Am. Mineral.* **70**, 1262 (1985).
- ⁷⁹ S. Peulon, Q. Baraize, A. Chausse, *Electrochimica Acta*, **52**, 7681–7688 (2007).
- ⁸⁰ S. J. Palmer, B. J. Reddy, R. L. Frost, *Spectrochimica Acta Part A*, **71**, 1814–1818 (2009).
- ⁸¹ L. Capek, V. Kreibich, J. Dedecek, T. Grygar, B. Wichterlova, Z. Sobalik, J.A. Martens, R. Brosius, V. Tokarova, *Microporous Mesoporous Mater.* **80**, 279 (2005).
- ⁸² J. Perez-Ramirez, J. C. Groen, A. Brückner, M. S. Kumar, U. Bentrup, M. N. Debbagh, L. A. Villaescusa, *J. Catal.* **232**, 318 (2005).
- ⁸³ M. Schwidder, M. S. Kumar, K. Klementiev, M. M. Pohl, A. Brückner, W. Grünert, *J. Catal.* **231**, 314 (2005).
- ⁸⁴ M. S. Kumar, M. Schwidder, W. Grünert, U. Bentrup, A. Brückner, *J. Catal.* **239**, 173 (2006).
- ⁸⁵ P. Balle, B. Geiger, S. Kureti, *Appl. Catal. B*, **85**, p. 109, (2008).
- ⁸⁶ M. Schwidder, S. Heikens, A. De Toni, S. Geisler, M. Berndt, A. Brückner, W. Grünert, *J. Catal.* **259**, 96 (2008).

- ⁸⁷ J. Gurgul, K. Łatka, I. Hnat, J. Rynkowski, S. Dzwigaj, *Microporous and Mesoporous Materials*, **168**, 1–6 (2013).
- ⁸⁸ G. R. Hunt, R. P. Ashely, *Econ. Geol.* **74**, 1613 (1979).
- ⁸⁹ M. D. Dyar, C. McCammon, M. W. Schaefer (Eds.), *The Geochem., Soc. Special Pub.* **5**, 23. (1996).
- ⁹⁰ J. L. Bishop, E. Murad, *Am. Mineral.* **90**, 1100 (2005)
- ⁹¹ N. S. Hush, F. A. Cotton (Ed.), *Progress in Inorganic Chemistry*, vol. 8, Interscience Publishers, New York, 391 (2006)
- ⁹² M. S. Kumar, M. Schwidder, W. Grünert, U. Bentrup, A. Brückner, *J. Catal.* **227**, 384 (2004).
- ⁹³ N. Griffete, M. J. D. Clift, A. Lamouri, R. G. Digigow, A. M. Mihut, A. Fink, B. Rothen-Rutishauser, H. Dietsch, *Colloids and Surfaces A: Physicochem. Eng. Aspects*, **415**, 98–104 (2012).
- ⁹⁴ C. Hoskins, L. Wang, W. P. Cheng, A. Cuschieri, *Nanoscale Research Letters*, **7**, 77 (2012).
- ⁹⁵ A. H. Lu, E. L. Salabas, F. Schuth, *Angew Chem Int Ed.* **46**, 1222 (2007).
- ⁹⁶ J. Gautier, E. Munnier, A. Paillard, K. Hervé, L. Douziech-Eyrolles, M. Soucé, P. Dubois, I. Chourpa, *International Journal of Pharmaceutics*, **423**, 16–25 (2012).
- ⁹⁷ S. Zhang, L. Zou, D. Zhang, X. Pang, H. Yang, Y. Xu, *J Nanopart Res.* **13**, 3867–3876 (2011).
- ⁹⁸ M. Kim, J. Jung, J. Lee, K. Na, S. Park, J. Hyun, *Colloids and Surfaces B: Biointerfaces*, **76**, 236–240 (2010).
- ⁹⁹ T. Neuberger, B. Schopf, H. Hofmann, M. Hofmann, B. V. Rechenberg, *J Magn Magn Mater.* **293**, 483–496 (2005).
- ¹⁰⁰ D. Patel, A. Kell, B. Simard, B. Xiang, H. Y. Lin, G. Tian, *Biomaterials*, **32**, Issue 4, 1167–1176 (2011).
- ¹⁰¹ R. Weissleder, A. Moore, U. Mahmood, R. Bhorade, H. Benveniste, E. A. Chiocca *et al.*, *Nat Med.* **6**, 351–354 (2000).
- ¹⁰² Y. M. Huh, Y. W. Jun, H. T. Song, S. Kim, J. S. Choi, J. H. Lee *et al.*, *J Am Chem Soc.* **127**, 12387–12391 (2005).
- ¹⁰³ T. Ahmad, H. Bae, I. Rhee, Y. Chang, J. Lee, S. Hong, *Current Applied Physics*, **12**, Issue 3, 969–974 (2012).
- ¹⁰⁴ A. K. Gupta, M. Gupta, *Biomaterials*, **26**, 3995–4021 (2005).
- ¹⁰⁵ Y. Lee, H. Lee, Y. B. Kim, J. Kim, T. Hyeon, H. W. Park, P. B. Messersmith, T. G. Park, *Adv. Mater.* **20**, 4154–4157 (2008).
- ¹⁰⁶ M. Mahmoudi, A. Simchi, A.S. Milani, P. Stroeve, *Journal of Colloid and Interface Science* **336**, 510–518 (2009).
- ¹⁰⁷ L. Menichetti, D. De Marchi, L. Calucci, G. Ciofani, A. Menciassi, C. Forte, *Applied Radiation and Isotopes* **69**, 1725–1727 (2011).
- ¹⁰⁸ M. Vallet, P. Rodriguez, X. Obradors, A. Isalgue, J. Rodriguez, M. Pernet, *JOURNAL DE PHYSIQUE C6*, **09**, 46, C6-335 (1985).
- ¹⁰⁹ M. D. Shultz, S. Calvin, P. P. Fatouros, S. A. Morrison, E. E. Carpenter, *Journal of Magnetism and Magnetic Materials*, **311**, 464–468 (2007).

